

Mean Offshore Refractive Conditions during the CASPER East Field Campaign

MARCELA ULATE^a

National Research Council, Washington, D.C., and Naval Postgraduate School, Monterey, California

QING WANG

Naval Postgraduate School, Monterey, California

TRACY HAACK AND TEDDY HOLT

Naval Research Laboratory, Monterey, California

DENNY P. ALAPPATTU

Naval Postgraduate School, Monterey, and Moss Landing Marine Laboratories, Moss Landing, California

(Manuscript received 31 January 2018, in final form 15 December 2018)

ABSTRACT

In this study, we use observational and numerical model data from the Coupled Air Sea Processes and Electromagnetic Ducting Research (CASPER) field campaign to describe the mean refractive conditions offshore Duck, North Carolina. The U.S. Navy operational numerical weather prediction model known as the Coupled Ocean–Atmosphere Mesoscale Prediction System (COAMPS) performed well forecasting large-scale conditions during the experiment, with an observed warm bias in SST and cold and dry biases in temperature and humidity in the lowest 2000 m. In general, COAMPS underpredicted the number of ducts, and they were weaker and at lower height than those seen in observations. It was found that there is a noticeable diurnal evolution of the ducts, more over land than over the ocean. Ducts were found to be more frequent over land but overall were stronger and deeper over the ocean. Also, the evaporative duct height increases as one moves offshore. A case study was chosen to describe the electromagnetic properties under different synoptic conditions. In this case the continental atmospheric boundary layer dominates and interacts with the marine atmospheric boundary layer. As a result, the latter moves around 80 km offshore and then back inland after 2 h.

1. Introduction

The Coupled Air Sea Processes and Electromagnetic Ducting Research (CASPER) field campaign CASPER East took place from 10 October to 6 November 2015

offshore Duck, North Carolina. Among CASPER East scientific goals is to study the surface layer and inversion dynamics over coastal regions, as well as the evolution of the electromagnetic (EM) propagation properties over the coast–ocean transition regions (Wang et al. 2018). In this work we describe the mean EM properties during CASPER East.

The speed at which EM waves propagate through the atmosphere is greatly affected by the vertical distribution of temperature and humidity. Each frequency's speed is characterized by the atmospheric refractive index N . Following Bean and Dutton (1966), N in N units is defined as

$$N = 77.6 \frac{P}{T} - 5.6 \frac{e}{T} + 3.75 \times 10^5 \frac{e}{T^2}, \quad (1)$$

^o Denotes content that is immediately available upon publication as open access.

^a Current affiliation: University Corporation for Atmospheric Research, Monterey, California.

Corresponding author: Marcela Ulate, marcela.ulate.ctr@nrlmry.navy.mil

where P is pressure (hPa), T is temperature (K), and e is vapor pressure (hPa). The modified refractive index M is defined as follows to account for Earth's curvature (Turton et al. 1988):

$$M = N + 0.157z, \quad (2)$$

where z is the height above sea level (m). Variations of the refractive index with height from the normal atmosphere result in different refractive phenomena. The regimes are named from the values of the change of M (or N) with height, dM/dz (M units km^{-1}).

The normal¹ refraction range in the atmosphere occurs between $79 \leq dM/dz \leq 157 M$ units km^{-1} . Subrefraction and superrefraction will occur when $dM/dz > 157$ and $0 < dM/dz < 79$, respectively. In this study we focus on ducting conditions only, since they play an important role in trapping EM energy and producing long “over the horizon” signals. A duct occurs when $dM/dz \leq 0$. Depending on the height of an EM source and the location of the target relative to the duct layer, signals can propagate over longer distances or be rapidly attenuated allowing for targets to be hidden. The top of the trapping layer is where M is a local minimum value M_{\min} , and the base of the trapping layer is the height at which the sign of dM/dz switches from positive to negative. The EM duct includes the trapping layer and extends below it to where $M = M_{\min}$ at the duct-base height (see Fig. 1 from Burk and Thompson 1997). Depending on the duct-base height and the trapping-layer height, an electromagnetic duct can be a surface-based duct, elevated duct, or a surface S-shaped duct [see Turton et al. (1988) for a detailed description on duct types]. The duct strength is the difference between the maximum and the minimum value of M within the duct.

Another type of duct briefly discussed in this paper is the evaporation duct, which is a ubiquitous feature that occurs within the lowest 50 m above the ocean surface. They occur due to strong gradients of humidity within the surface layer above the ocean that translate to changes in the M profile (Babin et al. 1997). Since the evaporation ducts occur within the first 50 m above the ocean, their characteristics, height, strength, and shape cannot be routinely determined from atmospheric profiles or soundings. In most cases, a parameterization is used to calculate the temperature and humidity profiles, after which M can be calculated. The evaporation duct height is then determined to be the region below the minimum value of M within that layer.

The East Coast of the United States is an area ripe for the study of EM ducts and their evolution (Meyer 1971;

Babin 1995, 1996; Haack et al. 2010; Wang et al. 2011; Thompson and Haack 2011). In this area the distribution of different surfaces (land, coast, cold ocean, and Gulf Stream) influences how the marine atmospheric boundary layer (MABL) behaves under different mesoscale conditions and where the ducts form (Thompson and Haack 2011), including effects from the advection of continental air over the cold ocean surface and advection across the Gulf Stream sea surface temperature (SST) front from warm to cold water (Thompson and Haack 2011). Therefore, this region has been the focus of several different studies and field campaigns. CASPER is the first study in which concurrent measurements of propagation and environmental variables are taken simultaneously to obtain a “snapshot” of the state of the atmosphere for a prolonged period of time.

Most of the previous EM studies along the eastern seaboard of the United States took place on or close to the NASA Wallops Flight Facility on Wallops Island, Virginia (Babin 1995, 1996; Thompson and Haack 2011; Haack et al. 2010), which is located ~ 117 miles north of the CASPER study area. Earlier studies were mainly case studies that were based primarily on observations. Babin (1996) analyzed 10 years of helicopter sounding profiles over and offshore Wallops Island and outlined a duct climatology. He found that surface ducts occur in the region around 70% of the time. In the same study it was also shown that the mean surface duct height increases during the year from 23.9 m during October–December up to 51.8 m during July–September and that the mean duct height increases in the afternoon by ~ 7 m throughout the year.

More recent studies document large horizontal and temporal variability in ducting conditions within the region using a combination of observations and numerical modeling (Haack et al. 2010; Thompson and Haack 2011). Haack et al. (2010) used buoy data, helicopter profiles, and numerical model forecasts as part of a multiagency field campaign, the Wallops 2000 Microwave Propagation Measurement Experiment. Haack et al. (2010) showed that the numerical models had a moist and cold bias close to the surface, which tends to produce weaker and fewer ducts when compared with the observations. They also concluded that to better predict atmospheric duct formation the numerical models have to use improved initial conditions, have higher vertical and horizontal resolution (less than 5 km), use evolving SST fields at a resolution close to their atmospheric counterpart, and have better data assimilation techniques for humidity observations. Moreover, Thompson and Haack (2011) studied the role of SSTs on microwave refractivity and found that diurnal variations in SSTs affect the initiation, timing, and frequency of ducting

¹The “standard atmosphere” value used for dM/dz is $118 M$ units km^{-1} .

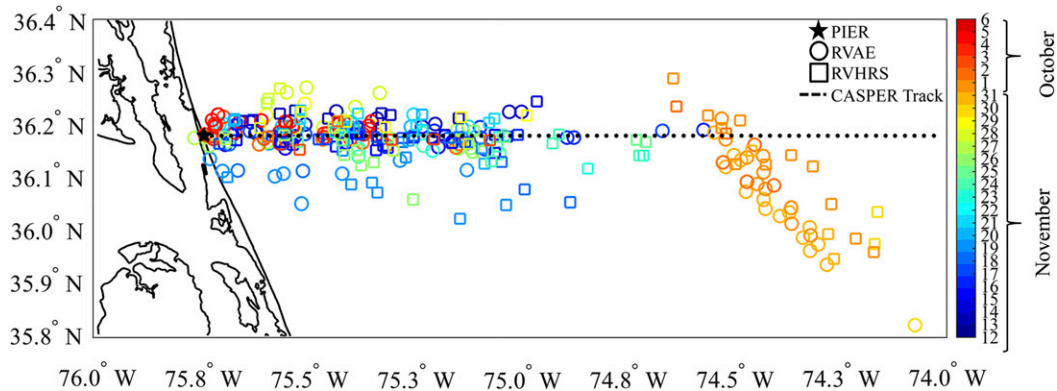


FIG. 1. Location of the sounding launching sites during CASPER East. The star denotes the location of the pier at Duck. The circles and squares are the sounding locations launched from the RVAE and RVHRS, respectively. The dotted line is the CASPER track, which is the path that most mobile platforms followed during the experiment. The color bar to the right indicates launch date.

events, advocating for the need for two-way coupled air–sea simulations in the region.

An important result of these recent studies is that EM properties in the area are strongly affected by the changing large-scale atmospheric conditions as well. Haack et al. (2010) found that high pressure and offshore-flow events were linked to stronger and weaker ducting conditions, respectively, and Thompson and Haack 2011 described how continental air advection has been found to be crucial in determining the favorableness for developing ducts. The conclusions from these studies rely heavily on numerical models.

Despite the fact that there have been many numerical studies on the evolution of ducts for different regions around the globe, one of the main hurdles to forecasting EM ducting lies in model resolution and the surface layer and the planetary boundary layer parameterizations. Often the surface layer schemes are formulated using Monin–Obukhov similarity theory (MOST; Monin and Obukhov 1954), which exhibits large uncertainty in near-neutral and stable surface forcing. In addition, the ability to adequately capture the inversion layer and its thickness is also a limiting factor in capturing elevated ducts.

In this study we use observations and numerical model forecasts from the CASPER East experiment. Numerical model data are compared with observations. We then use the model results to describe the interactions between the different air masses close to the coast and their effect on the duct formation and evolution for a case study. In section 2 we describe the data and the method used. In section 3 we discuss the numerical model evaluation and the mean EM conditions during CASPER East, and last we discuss the conditions during 20 October 2015. Conclusions and final remarks are given in section 4.

2. Data and methods

The CASPER East field campaign took place from 10 October to 6 November 2015 offshore Duck. This field campaign was set up so that simultaneous measurements of the environment and EM propagation were taken in the region (Wang et al. 2018). Measurements were taken at the coast (the Duck pier), over the ocean (by two research vessels, surface buoys, and underwater gliders), and in the air (by two research aircraft). Most ocean and air observations were taken along the CASPER East track (Fig. 1). The CASPER East track is the path that most mobile platforms followed during the experiment (Wang et al. 2018). Surface fluxes, radiation, and atmospheric turbulence were measured at various vertical levels at the pier and over the ocean (Wang et al. 2018). There were also receivers and antennas used to measure refractivity and EM properties through the lower atmosphere during coordinated efforts between stationary (pier) and moving (ship) observation platforms. In this study we use data from four sources: radiosondes, surface stations (measured at the bow mast of one of the ships), SST, and tethered-balloon data.

The radiosondes were launched from the Duck pier and from two research vessels: the *Atlantic Explorer* (RVAE) and the *Hugh R. Sharp* (RVHRS). RVHRS and the RVAE left port on 11 October 2015 and arrived to the CASPER East site on 11 and 12 October 2015, respectively. RVHRS and RVAE were deployed in the field until 3 and 5 November 2015, respectively. During this time there was one port call for both research vessels on 22 October 2015. On 28 October 2015 RVHRS had to leave the CASPER East area of study to refuel.

The soundings launched from RVAE and RVHRS were released at specific locations along the CASPER

track offshore Duck (Fig. 1). Pier and ship soundings were launched during coordinated efforts to maximize the amount of simultaneous snapshots of the distribution of ducts at different times along the CASPER track.

A total of 372 soundings were launched during the CASPER field campaign. Of these, 159 were deployed from RVAE, 137 were deployed from RVHRS, and 76 were launched from the Pier at Duck (Fig. 1). In this study we use 360² soundings that were launched between 12 October 2015 and 4 November 2015. The sounding data correspond to upward soundings only. The mean elevation that the soundings reached was ~4500 m. Therefore, we focus on quantitative comparisons up to 5 km.

Bow-mast data were collected from sensors mounted ~12 m above the water line on the RVHRS. Measurements of temperature, humidity, pressure, and winds were taken at a temporal resolution of 20 Hz. We used hourly averages of these data. The SST data were also taken from RVHRS. These are a composite between measurements on an autonomous infrared radiometer probe and the bulk SST taken by a sensor in the RVHRS. The composite is a three-step procedure that corrects for effects from wind, the diurnal cycle, and longwave radiation flux (Alappattu et al. 2017).

Vertical profiles of temperature, humidity, and pressure for the first 50 m were obtained by moving an Allsopp Helikites, Ltd., Helikite tethered balloon with radiosondes tied to its end up and down from a small rigid-hull inflatable boat. The radiosondes were located 2 m from each other up to 10 m, and measurements were taken every 2 s. The small boat was deployed from the RVHRS to avoid flow distortion.

The sampling procedure from Kang and Wang (2016) and Alappattu et al. (2016b) was followed, and several measurements were taken at different vertical levels at one location; from them a unique “fitted” profile was obtained. The fitted profiles were used to calculate the evaporative duct height directly from observations. A total of 41 vertical profiles in different locations were obtained during the field campaign. Although the dataset during CASPER East is not particularly large, it is larger than other datasets used on similar studies. However, the length of the dataset should be taken in to account and be noted as one of the limitations of this study. Basic statistical tests were calculated to estimate the significance of our results (see section 3).

²The 12 soundings not included were launched between 5 November (11) and 6 November (1) 2015 from the RVAE. They were not included because the last COAMPS forecast was at 1200 UTC 4 November 2015.

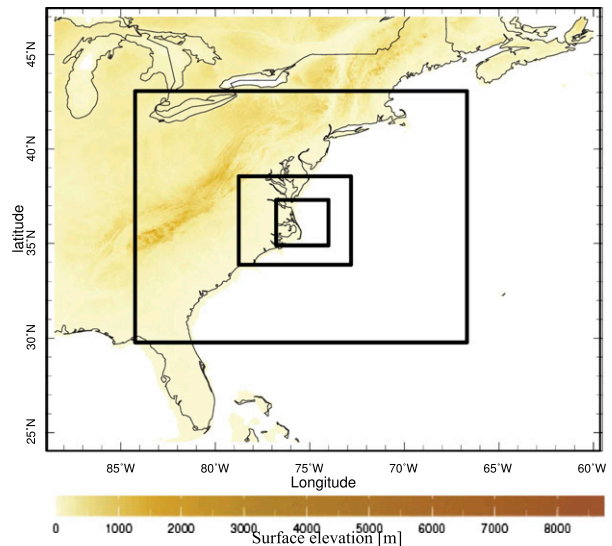


FIG. 2. COAMPS atmospheric domains during CASPER East. The domains have 54-, 18-, 6-, and 2-km horizontal resolution with 70 vertical levels. Topography is shown on the grids.

a. Numerical simulations

During CASPER, high-resolution numerical weather prediction forecasts by the U.S. Navy’s Coupled Ocean–Atmosphere Mesoscale Prediction System (COAMPS; Hodur 1997)³ were made to forecast environmental and ducting conditions over the region and to support CASPER’s research vessel and platform operations. COAMPS was run as a fully two-way coupled air–ocean system. The atmospheric model is nonhydrostatic, has a vertically stretched terrain-following vertical grid, and employs a semi-implicit time-splitting technique for efficient computations of the acoustic modes of the compressible equations, following the method of Klemp and Wilhelmson (1978). Each horizontally nested grid has 3 times the resolution of its parent grid. For numerical weather prediction modeling focused on marine and boundary layer vertical gradients, over coastal and littoral regions, or involving refractive effects, minimum resolution requirements have been established of 4-km horizontal grid spacing and 60-m average vertical grid spacing in the MABL and planetary boundary layer (Haack et al. 2010). These requirements were met for COAMPS fully coupled air–sea model forecasts performed in real time for CASPER East such that the inner nest had 2-km grid spacing (parent nests had 54-, 18-, and 6-km resolution), and the 70 vertical levels averaged 60 m in the lowest 1 km. Figure 2 shows the

³COAMPS is a registered trademark of the Naval Research Laboratory.

domain configuration for the atmospheric component in COAMPS for CASPER East.

Atmospheric physics options for COAMPS mesoscale simulations were set such that moist convection is explicitly resolved at grid resolutions less than 10 km. Thus, all microphysical processes, conversions between moisture species, and the associated diabatic adjustments in temperature are determined by an updated Rutledge and Hobbs (1983) scheme that was modified for drizzle and nonprecipitating clouds using Khairoutdinov and Kogan (2000) to include cloud condensation nucleus and cloud/drizzle drop concentrations appropriate for stratocumulus topped boundary layers. The subgrid-scale mixing scheme includes prognostic equations for turbulent kinetic energy based on Mellor and Yamada's (1982) 1.5-order closure, and surface fluxes are parameterized after Louis (1979) and Louis et al. (1982), utilizing advancements from the TOGA COARE as adapted for COAMPS by Wang et al. (2002). The long- and shortwave radiation is represented by a four-stream approximation for radiative transfer proposed by Fu and Liou (1993).

The ocean model configuration consisted of two nested grids of 9 and 3 km, and 50 vertical levels. The initialization fields were taken from the Navy global model (NAVGEN) and the Navy Coastal Ocean Model (NCOM) for the atmospheric and ocean initialization, respectively. The forecasts were run every 6 h with hourly outputs for 48 h at 0000 and 1200 UTC, and only 6-h outputs at 0600 and 1800 UTC.

For this study we use COAMPS analysis and the first 11 forecast hours for the 0000 and the 1200 UTC initiation times of the highest-resolution domain (2 km) concatenated together to make a 24-h forecast for each day. These composites are called a hindcast. COAMPS forecasts have performed well in other similar studies in this region (Haack et al. 2010; Thompson and Haack 2011). In Haack et al.'s (2010) study, COAMPS performed the best of four numerical models simulating ducting conditions extending offshore of Wallops Island, further justifying the use of this model.

In this study, COAMPS forecasts were compared with a select set of observations taken during CASPER. To obtain one-to-one comparisons between observations and gridded model data, the closest grid point to a specific location (and rounded to the nearest hour) was taken from the COAMPS gridded hindcast to match that observation. In the case of soundings, the location is considered to be the mean location during the lowest 300 m of ascent. The observational sounding data were then interpolated to the 70 vertical height levels in COAMPS and compared with the COAMPS profile.

To study the refractivity and EM properties, the duct strength, duct base, trapping layer, and duct height (which refers to the top of the duct) were calculated from vertical

profiles of M from soundings and from COAMPS data. The evaporative duct height from observations was obtained from the tethered-balloon data. The M profiles were calculated from the temperature and humidity tethered-balloon data. The evaporative duct height was set to be the height at which $dM/dz = 0$ in the first 50 m (i.e., first minimum of M within the first 50 m). The evaporative duct height from COAMPS was calculated by using 5-m pressure, temperature, humidity, winds, and the SST as input to the COARE bulk flux algorithm, version 3.0 (Fairall et al. 2003). This algorithm uses MOST to calculate surface fluxes; from those, the vertical profiles of various variables are reconstructed (Alappattu et al. 2016a) and M is calculated. In the literature, other methods to calculate evaporative ducts have been widely used, such as in Zhang et al. (2016, 2017). In their study, a three-parameter empirical model is proposed to obtain evaporative duct height information, and numerical model climatological data are used to obtain certain parameters from each location of study. This method was not applied in this research because the usage of another 32 years of data would be outside the scope of this paper.

Simple statistics were calculated to evaluate COAMPS's hindcast against observations. Such parameters include the bias,⁴ mean bias, standard deviation, root-mean-square error (rmse), and correlations. A paired-sample t test was performed to check the statistical significance of our results comparing observations and COAMPS data. Contingency statistics were also calculated to rate the EM duct height forecasts. These calculations were made using the interpolated observed sounding and the COAMPS soundings. For each observed sounding, the lowest duct (height ≤ 2 km) was found, and, from this, marginal totals for the forecasts were computed. The quantities calculated include hits, false alarms, misses, correct null or post-agreement, and probability of detection. Following Wilks (2011), a hit is defined as the fraction of the total forecasts that have or do not have ducts at the same time as the observational sounding within a height threshold, that is, ($\pm 50, \pm 100, \pm 200, \dots, \pm 2000$ m) up to 2000-m height. Miss rate is defined as $1 - \text{hits}$. The false alarm is the ratio of the COAMPS soundings that had ducts that were not present in the observations within a certain threshold. The correct null or postagreement is defined as $1 - \text{false-alarm ratio}$. Last, the probability of detection was computed as the ratio in which the duct was present in the observations and was forecast in COAMPS within a height threshold. The values of these contingency statistics at different thresholds

⁴ Bias is here defined as the difference between COAMPS and the observations at a particular location and at each vertical level.

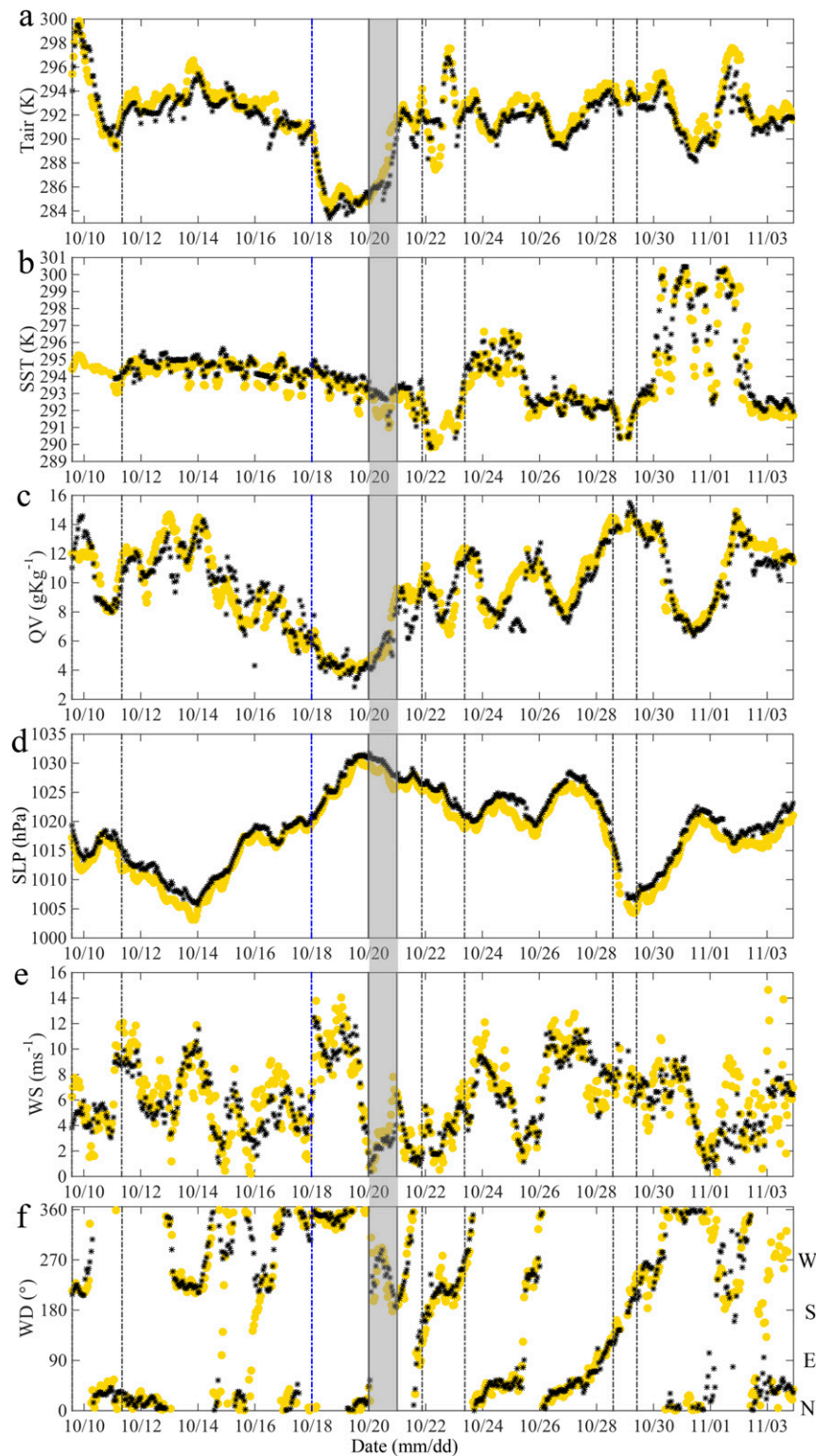


FIG. 3. Time series of (a) air temperature (K), (b) SST (K), (c) water vapor mixing ratio ($g\ kg^{-1}$), (d) sea level pressure (hPa), (e) wind speed ($m\ s^{-1}$), and (f) wind direction ($^{\circ}$) from bow-mast data from RVHRS (yellow) and from COAMPS hindcasts (black). The vertical gray lines and shaded-gray area denote the case-study date (20 Oct). The sets of dashed vertical gray lines indicate the periods during which the RVHRS was out of the CASPER supersite (port before the start of the experiment, port call, and refueling). The dashed blue lines

and their implications on how we evaluate numerical model duct forecasts are discussed in the results section.

3. Results

a. COAMPS evaluation

COAMPS forecasts were compared with bow-mast data to assess model skill to forecast the general synoptic conditions during CASPER East. Figure 3 shows the time series for six different variables compared to COAMPS hindcast data. Overall COAMPS compares well to observations during the experiment and follows the general trends in temperature, SST, humidity, pressure, and wind (Fig. 3). COAMPS is able to capture many of the abrupt changes seen in the observations. One example is the cold-frontal passage from 18 to 21 October (Fig. 3). During this period, both observations and COAMPS show the coldest temperatures for the entire 3-week period as well as an increase in wind speed and decrease in humidity. COAMPS also compares favorably to observations from 30 October to 3 November, when the RVHRS took measurements over the Gulf Stream. During this period, observed SST increases significantly, which was captured by COAMPS. However, COAMPS shows a much smoother transition than the observations as it crosses the Gulf Stream. As an example, on 30 October 2015, as the RVHRS moves from cooler to warmer temperatures close to the Gulf Stream, two observations separated by 13.47 km (36.01°N, -74.13°W and 35.96°N, -74.00°W) have a difference in SST of 4.40 K whereas in COAMPS the distance was 13.71 km (36.01°N, -74.14°W and 35.96°N, -74.00°W) and the difference was 1.87 K (see 30 October 2015 in Fig. 3). In measurements taken closer to the coast, away from the Gulf Stream SST front, the difference between observations and COAMPS is not as pronounced. As an example, on 29 October 2015 the observations reported -0.03 K difference over a 12.3-km distance (36.18°N, -75.33°W and 36.18°N, -75.19°W), COAMPS hindcasts reported -0.14 K difference over a 14.31-km distance (36.18°N, -75.34°W and 36.18°N, -75.18°W). Overall, the mean distance between all of the observation locations is 6.27 km (6.34 km for COAMPS) with a difference in SSTs of

TABLE 1. Statistical parameters comparing RVHRS bow-mast and SST data with COAMPS hindcasts. All of the data points, including while the RVHRS was in port, are included on the calculation of the parameters (see Fig. 3).

	Bias	rmse	Correlation	No. of points
Air temperature (K)	-0.54	1.18	0.93	604
SST (K)	0.27	0.74	0.94	591
SLP (hPa)	1.56	1.80	0.99	604
Humidity (g kg ⁻¹)	-0.22	1.22	0.91	604
Wind speed (m s ⁻¹)	-0.26	2.16	0.74	604

-0.0049 K (-0.0046 K for COAMPS hindcasts), which makes the previous calculations stand out.

Mean surface statistics between observed and modeled parameters are reported in Table 1. A paired-sample *t* test was performed for the observations and the COAMPS data used to calculate the values in Table 1. All variables passed the test with 95% confidence level, which adds value to our dataset despite its short record. The air temperature and SST biases are -0.54 and 0.27 K, respectively, which indicates that COAMPS has a cold bias in temperature close to the surface and a warm bias in SST. Wang et al. (2011) found similar results in the southwestern Pacific Ocean. There is a positive bias in sea level pressure (SLP) of 1.56 hPa and negative biases for humidity (-0.22 g kg⁻¹) and wind speed (-0.26 m s⁻¹). Haack et al. (2010) compared COAMPS data with buoy data near Wallops Island and found similar results (note that their definition of bias is observation minus model) for air temperature (cold bias in COAMPS), SLP (higher SLP in COAMPS), and wind speed (weaker winds in COAMPS). Their results for SSTs and humidity differ from our results. In their study Haack et al. (2010) obtained a cold bias on model SSTs and a moist bias close to the surface (about -1.7% moister than the observations). A reason for the difference may be the fact that for CASPER East COAMPS was set up to have two-way coupling between the ocean and the atmosphere, which would make the SST errors decrease. Haack et al. (2010) reported a 0.6-K bias and 0.9-K rmse, whereas in this work we found 0.27-K bias and 0.74-K rmse. The version of COAMPS used in Haack et al. (2010) was one-way coupled (from ocean to atmosphere). Although the improvement in the SST forecast may be attributed to air-sea coupling, other

←

indicate the passage of the cold front (18 Oct). The first bow-mast data measurement was taken at 1400 UTC 9 Oct 2015 while RVHRS was in port, and the last one was taken at 2200 UTC 3 Nov 2015 before heading to port. The wind direction convention is the meteorological standard in which the direction from which the winds are coming is indicated, increasing from north (0°/360°) clockwise. One COAMPS data point was cropped from (e): for 29 Oct 2015 the winds speed measured in the bow-mast data were 6.00 m s⁻¹ whereas the COAMPS hindcast value was 30.23 m s⁻¹. This value was kept for the calculations presented in Table 1.

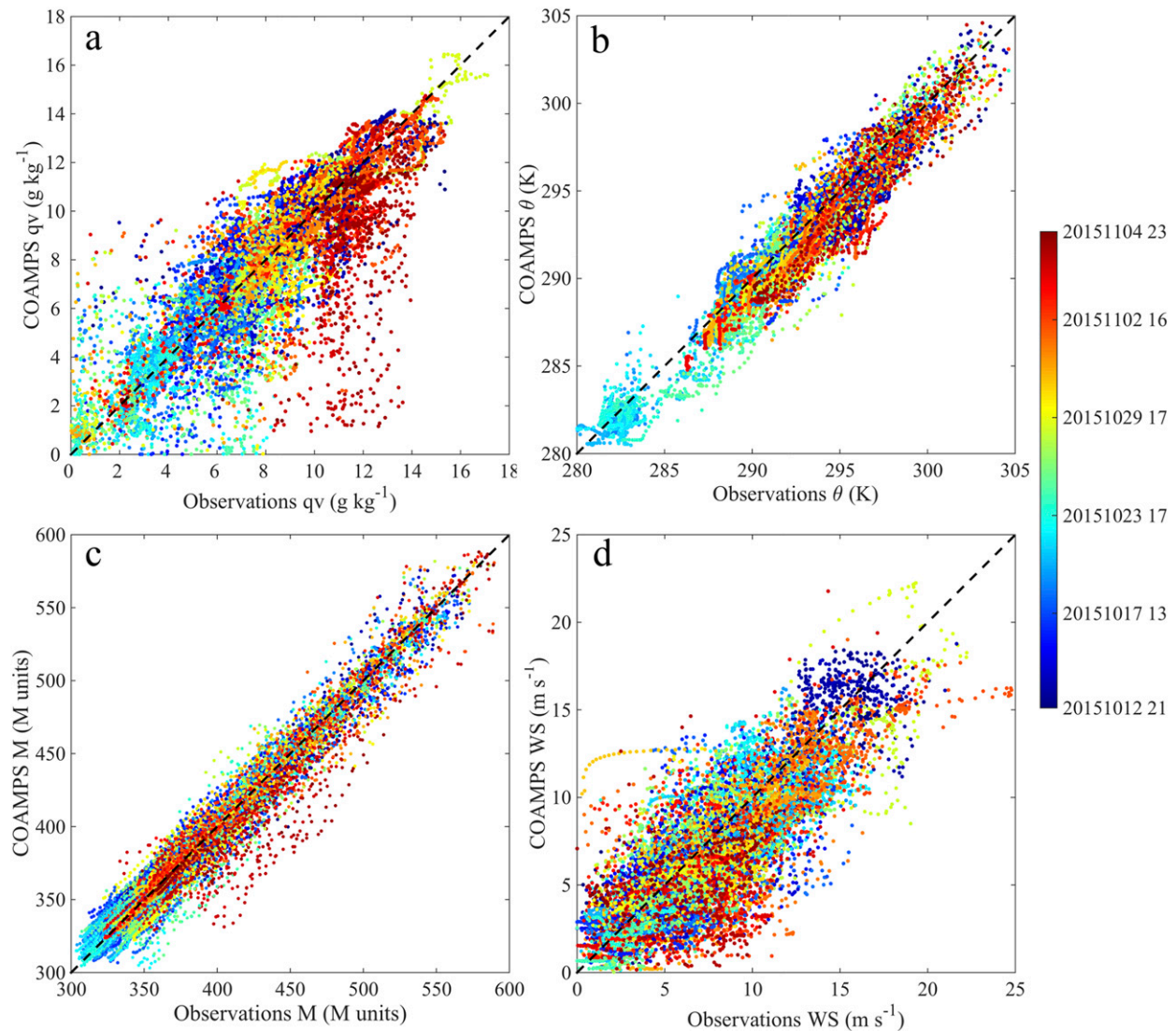


FIG. 4. Scatter diagrams of COAMPS vs observations of (a) water vapor mixing ratio (g kg^{-1}), (b) potential temperature (K), (c) modified refractivity (M units), and (d) wind speed (m s^{-1}) for heights of less than or equal to 2000 m. The colors represent the date of the data (as shown in the color bar). The number of points for each plot is the same as in Table 2.

factors could also play a role such as the amount of observational data, model resolution, time of year, model physics, and/or availability of new data sources since 2000. Regardless of the fact that Haack et al. (2010) reports different bias trends in COAMPS, their results also show that COAMPS does a better job than three other numerical models. In their study, COAMPS had the smallest bias and rmse at 5,⁵ 45, and 112 m for

specific humidity and at 45 and 112 m for M . COAMPS also had the smallest biases in SST (0.6 K), near-surface air temperature (0.2 K), and wind speed (0.3 m s^{-1} ; Met Office model had a similar bias of -0.3 m s^{-1}), however, COAMPS forecasts were merely similar to other models for wind direction (where COAMPS bias was $\sim 25^\circ$ with respect to buoy measurements).

COAMPS forecasts were also compared with sounding data. Figure 4 shows the scatter diagrams for temperature, humidity, modified refractivity, and wind speed below 2000 m. The data in Fig. 4 correspond to COAMPS vertical profiles versus the sounding data for altitudes less than 2 km. Table 2 presents Fig. 4 statistics. Similar to the statistics shown in Table 1, a paired-sample t test was

⁵ At 5 m, the Canadian Global Environmental Multiscale model (GEM) specific humidity bias had the same absolute value but different sign (-0.1 g kg^{-1}) as the bias calculated for COAMPS (0.1 g kg^{-1}).

TABLE 2. Statistical parameters comparing sounding observations with COAMPS vertical profiles. A paired-sample *t* test was performed; entries in italic font indicate that the test was not statistically significant for that variable.

	Mean _{OBS}	Mean _{COAMPS}	σ_{OBS}	σ_{COAMPS}	Bias	σ_{BIAS}	rmse	Correlation	No. of points
<i>z</i> ≤ 2000 m									
Modified refractivity (<i>M</i> units)	399.56	399.01	16.08	16.14	−0.66	11.72	5.94	0.98	14 385
Water vapor mixing ratio (g kg ^{−1})	7.54	7.30	2.90	2.83	−0.26	1.71	0.86	0.85	14 385
Potential temperature (K)	291.49	290.93	4.08	3.92	−0.61	1.12	0.71	0.97	14 467
Wind speed (m s ^{−1})	7.83	7.07	3.95	3.76	−0.75	2.43	1.45	0.80	14 535
2000 < <i>z</i> < 5000 m									
Modified refractivity (<i>M</i> units)	728.88	730.13	12.69	12.73	0.65	6.61	3.08	1.00	1585
Water vapor mixing ratio (g kg ^{−1})	2.58	2.82	2.36	2.37	0.07	1.16	0.53	0.84	1585
Potential temperature (K)	307.18	307.40	3.91	3.49	−0.43	1.18	0.68	0.98	1602
Wind speed (m s ^{−1})	14.22	13.60	7.14	6.52	−0.17	2.80	1.53	0.93	1601

performed for the data, from which the values of Table 2 were obtained. For all of the variables, with the exception of one (water vapor mixing ratio between 2 and 5 km) the test passed with a 0.05 significance level. It is also important to notice that for Table 2 the number of data points for $z \leq 2$ km and $2 < z \leq 5$ km differs by a factor of 10 (Table 2) because of the model's vertical-level configuration, in which the lower altitudes have higher resolution: 42 versus 10 vertical levels.

Figure 4 shows the large range in observed values as an indicator of the variations in altitude but also in synoptic conditions during the field campaign (as seen in Fig. 3). These variations are quantified by the large values of water vapor mixing ratio, temperature, and wind speed standard deviation values (Table 2). The greatest differences in water vapor mixing ratio occur below 2000 m. This was well captured by COAMPS (see Table 2): below (above) 2000 m the observations had a standard deviation value of 2.90 (2.36) g kg^{−1}, which compares favorably to 2.83 (2.37) g kg^{−1} standard deviation values in COAMPS. However, the bias and rmse values are greater below 2000 m, a result that indicates the difficulty in accurately capturing the turbulent boundary layer processes. As mentioned previously, the statistics for water vapor mixing ratio between 2 and 5 km did not pass the *t* test. However, the results were kept in this discussion in hope of future studies finding them significant with additional data. The water vapor mixing ratio also has the second lowest correlation values: 0.85 (0.84) for sounding data below (above) 2 km and 0.91 for bow-mast data. This emphasizes again the difficult task that numerical models face in correctly predicting low-level humidity and, hence, refractivity.

The modified refractivity *M*, which is closely linked to the humidity, shows the same behavior as water vapor mixing ratio, with a larger negative bias below 2000 m: −0.66 *M* units versus a positive bias above: 0.65 *M* units. The mean biases below and above 2000 m are considerably smaller than the deviations of the observations

(16.08 *M* units) and from COAMPS (16.14). The scatter diagram of *M* also shows overall good agreement (Fig. 4c), with a 0.98 correlation coefficient below 2 km (Table 2), which agrees with Thompson and Haack (2011) who reported a correlation of 0.7. Also, *M* has the highest correlation coefficient below 2000 m of any of the sounding variables analyzed here. This result generates confidence in the evolution and location of the EM-ducts and modified-refractivity forecasts in COAMPS relative to the observations. Last, the scatter diagram for the wind speed shows large variations between observations and COAMPS. The correlation coefficient is the lowest of the variables analyzed: 0.80 for the sounding data below 2 km (Table 2) and 0.74 for the bow-mast data (Table 1). Overall, COAMPS underestimates the wind speed with a mean bias below (above) 2000 m of −0.75 m s^{−1} (−0.17 m s^{−1}) and slightly greater errors above 2 km (see Table 2). In this case, small changes in the strength or location of the jet stream can lead to large errors at higher altitudes. Our results show that COAMPS has a cold bias: −0.61 K below 2 km and −0.43 K between 2 and 5 km. We believe this is due to a lower and at times thinner inversion layer. Wang et al. (2011) found similar results in the southeastern Pacific: temperature bias of −0.7 K and rmse of 0.5 K. This indicates that there may be a model intrinsic error in the boundary layer.

The standard deviation between model and observations σ_{BIAS} is less than the differences between observations σ_{OBS} and COAMPS σ_{COAMPS} alone for all variables (see Table 2). This result indicates that the differences between observations and COAMPS are smaller than the variations among observations and model results, which reiterates that the numerical model errors are smaller than the day-to-day variations in synoptic conditions. The mean values of temperature, water vapor mixing ratio, wind, and modified refractivity presented in Table 2 are also a good indication of the similarities between the observations and the COAMPS profiles.

Figure 5 shows the vertical profile of the mean bias (model – observation) for each level up to 5 km, as well as the 10th and 90th percentile of the 360 soundings used to calculate such bias. The standard deviation of the bias and the rmse are also shown. In the case of humidity, COAMPS underestimates the water vapor mixing ratio below 2000 m (see Fig. 5a). This result is reflected in the value of the mean vertical bias of -0.26 g kg^{-1} (see Table 2). There is also a maximum (negative) bias of roughly -0.75 g kg^{-1} near 1000 m. Our results also show a small overestimation of the humidity in some of the layers closest to the surface. Haack et al. (2010) reported an overestimation of humidity in the MABL. In our case we find an underestimation (bias = -0.15 g kg^{-1} ; rmse = 0.68) in the model level closest to the surface (5 m) and overestimation up to 174 m (13th model level; see Fig. 5a). By comparing similar vertical levels with those shown in Haack et al. (2010), our results show biases (rmse) values in water vapor mixing ratio at 50 and 104 m of 0.05 (0.63) and 0.02 (0.65) g kg^{-1} , respectively. These values are smaller than those found in Haack et al. (2010), for all rmse and bias; however, the mean observational (9.23, 8.78, and 8.65 g kg^{-1}) and forecast values (9.10, 8.81, and 8.65 g kg^{-1}) at 5, 50, and 104 m indicate a moister boundary layer just above the surface. The differences between our results and Haack et al. (2010) may be due differences in year, season, and the location of the data and observational sources.

As expected, M biases closest to the surface also follow the shape of the humidity bias profile (see Fig. 5c), with mostly underestimation values of M below 2000 m. However, there is a very small overestimation in the lowest five model levels (5–50 m). The mean value of the M bias below 2000 m is $-0.66 M$ units; however, the rmse is small and correlations are close to 1.0 (see Table 2). The lines for the 10th and 90th percentiles also follow a shape that is similar to that of the mean bias (M and water vapor mixing ratio), with greater differences between 500 and 2000 m and skewed toward negative values. The spread of the bias also decreases with height, differently than the temperature and the winds, where the spread of the differences remains fairly constant in the vertical direction (not shown). In the case of temperature, our results show underestimation of the sounding temperature throughout the vertical plane (see Fig. 5b). There is a negative temperature bias with large values close to the surface of roughly -0.95 K (close to 5 m) and around -0.7 K at 5000 m (see Fig. 5b). In the mean, below and above 2000 m the temperature biases are small, -0.61 and -0.43 , with correlation values close to 1 (see Table 2). This can also be seen in the closeness of the points to the one-to-one line in Fig. 4b. The wind speed biases were also plotted in Fig. 5d. COAMPS underestimates the wind speed for

almost all vertical levels with the exception of the first two levels closest to the surface, where the differences are close to 1.0 ms^{-1} . The winds also have the lowest correlation coefficient (Table 1: 0.74; Table 2: 0.80 and 0.93), suggesting greater forecast difficulty. In general the biases are greater in the zonal direction.

Electromagnetic ducts detected in COAMPS versus those detected from the interpolated soundings⁶ were also compared. The advantage of using the interpolated soundings is that a fair comparison between COAMPS and soundings can be done. The disadvantage is that if the ducts are thin they may be unaccounted for. In fact, the number of ducts found in the observations decreased by $\sim 47\%$ when the interpolated data were used, and the majority were within the first 200 m. The ducts found in the interpolated and COAMPS soundings are limited by their vertical resolution.

Duct height and strength shown in Fig. 6 for the sounding locations indicate COAMPS compares well to observations. Seventy EM ducts were found for RVAE, 65 for RVHRS, and 53 for those launched from the pier. In total 45.22% of the total soundings presented electromagnetic ducts with height of less than 2 km. At the beginning of the field campaign (first 6–8 days), there is an underestimation in the number of ducts and their height, especially for soundings close to the coast (Fig. 6c). This could be because of vertical-resolution issues or time averaging within the model, especially if the ducts are short lived in the observations. COAMPS also seems to better forecast the height and depth of the ducts formed over the ocean (Figs. 6a,b) than those formed close to the coast (Fig. 6c). Note that the numerical model is limited by its output frequency, which in this case is 1 h, whereas the observations do not have any time restrictions. Therefore, we are comparing in situ observations (in time and space) with the closest grid point and hourly time in COAMPS. Such assumptions may result in an underestimation of the ducts forecast by COAMPS, especially if they are short-lived features. Taking those limitations into account, our results show that for some cases COAMPS forecasts miss the duct while in other cases COAMPS forecasts ducts that fail to occur in the observations. However, for other cases the forecast agrees extremely well with observations. There are two periods of time when COAMPS better predicted ducting conditions offshore⁷: 1) from 2000 UTC 19 October to 1700 UTC 27 October for RVAE (Fig. 6a) and from 2100 UTC 19 October to

⁶ Soundings were interpolated to COAMPS vertical levels.

⁷ Soundings over the research vessels were compared with COAMPS.

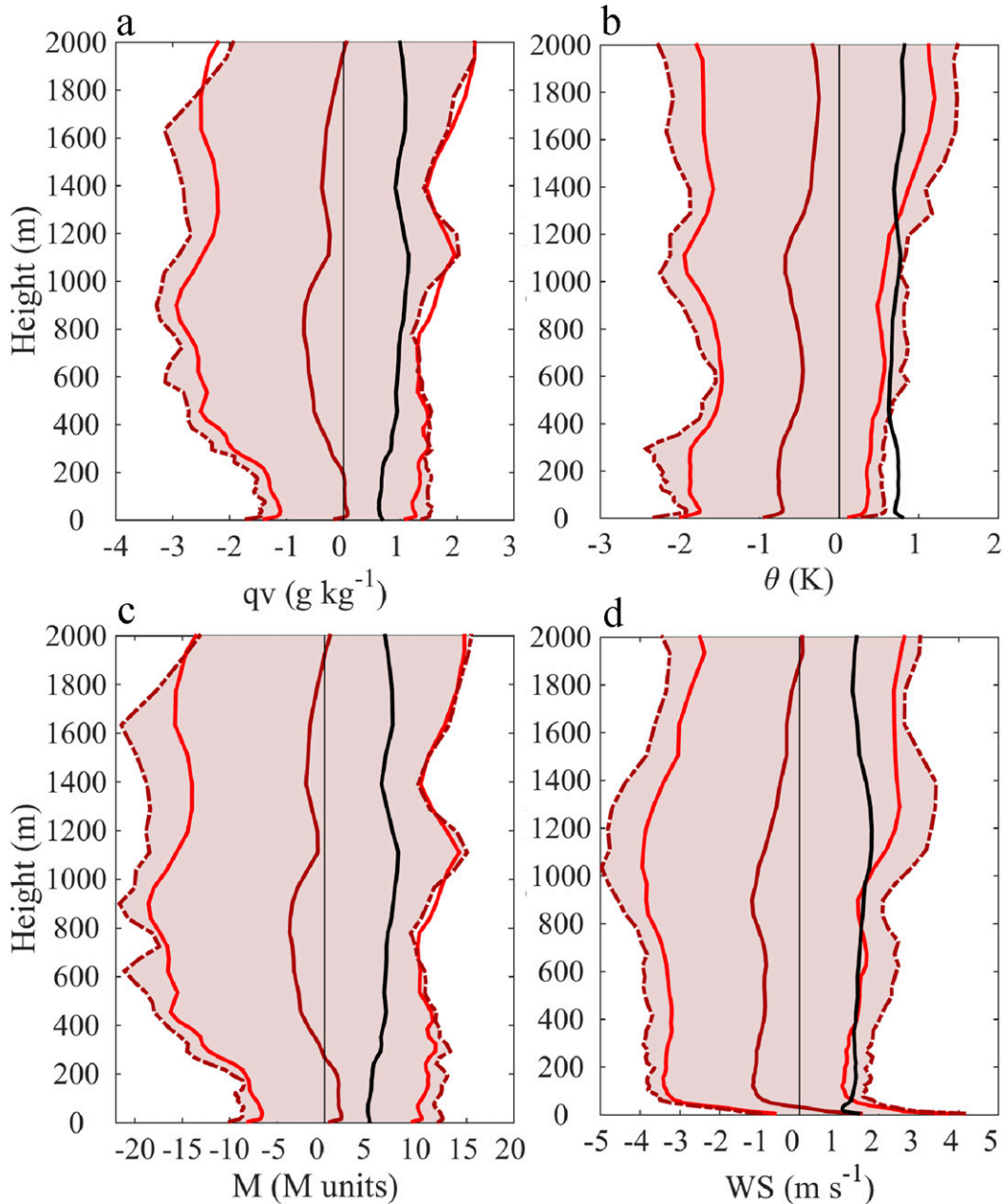


FIG. 5. Vertical profiles of mean bias (model – observation) for (a) water vapor mixing ratio (g kg^{-1}), (b) potential temperature (K), (c) modified refractivity (M units), and (d) wind speed (m s^{-1}). The red-shaded area represents the 10th and 90th percentile of the bias. The 10th and 90th percentiles are the dashed dark-red lines (edges of shaded area). The bright red lines are the \pm standard deviation of the bias. The solid dark-red line (in the middle of the shaded area) is the mean of the bias. The thick black line is the mean rmse. For each COAMPS level, the bias is composed of 360 points.

1200 UTC 28 October for RVHRS (see Fig. 6b) and 2) from 1700 UTC 29 October to 1600 UTC 2 November for RVAE (Fig. 6a). Of those soundings launched from the pier, the period from 2100 UTC 19 October to 2000 UTC 21 October stands out from Fig. 6c as a period for which the soundings were well forecast (Fig. 6c).

There is also a reduction in the number of ducts observed during the cold-frontal passage (18–20 October). Cold-frontal conditions are known to be unfavorable for duct development (Babin 1995). During this period, the number of ducts forecast by COAMPS also was reduced; however the model was not able to forecast a couple of

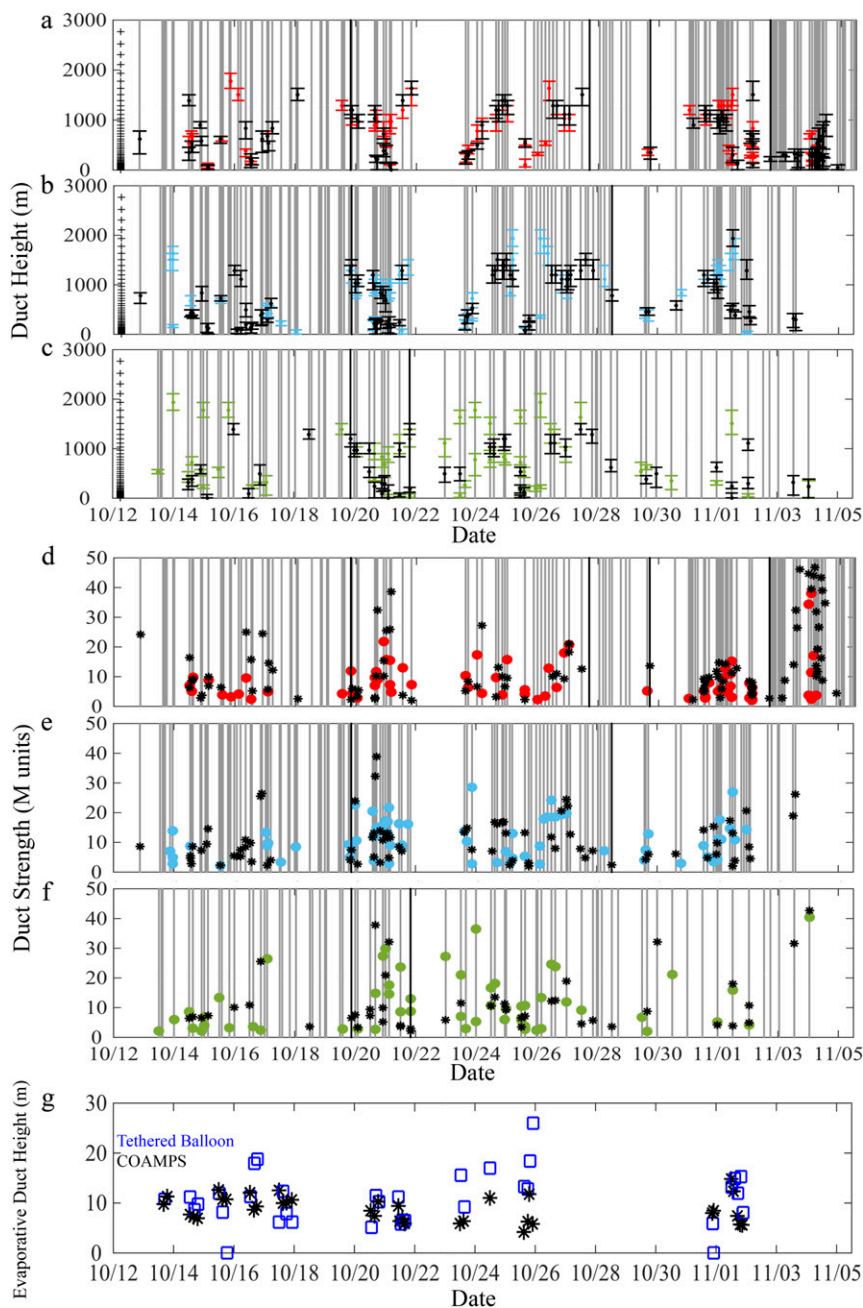


FIG. 6. (top) Duct height and (middle) duct strength computed from soundings launched from (a),(d) the RVAE (red), (b),(e) the RVHRS (light blue), and (c),(f) the pier (green) vs COAMPS data (black). The vertical gray lines indicate the times when soundings were launched. The duct height and strength were calculated using the soundings interpolated to the COAMPS vertical levels. (g) Evaporative duct height comparison between observations taken using a tethered balloon (blue) and COAMPS output (black).

the ducts that did form close to the surface (see Fig. 6b). Thompson and Haack (2011) also noticed poor model performance during a frontal passage in their study.

Differences in duct strength vary depending on the time period. In general, the magnitude of the strength

forecast by COAMPS is of the same order as in the soundings; however, there are some cases in which it is overestimated. For RVAE, from 1200 UTC 31 October to 1600 UTC 2 November shows forecast values of duct strength similar to observations (see Fig. 6d), whereas

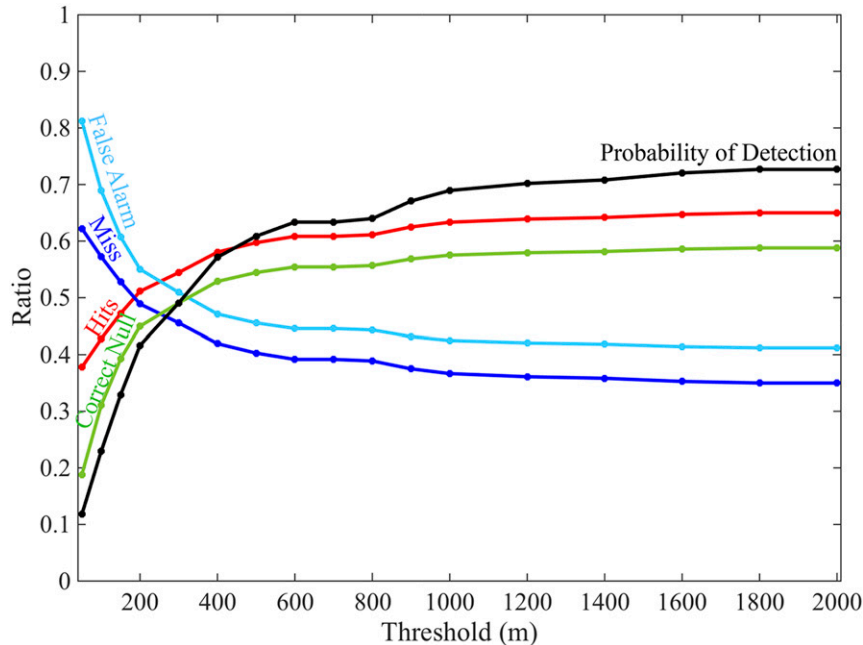


FIG. 7. Contingency statistics: probability of detection (black), false alarm (light blue), miss rate (dark blue), hits (red), and correct null (green) as a function of the threshold used to compare duct height.

the period after the 0300 UTC 3 November sounding shows an overestimation of duct strength. The evaporative duct heights obtained from the TOGA model (see section 2) using COAMPS forecast fields (Fig. 6g) are close to the observed values in the majority of the cases.

Contingency statistics for duct height were computed. The calculation of these variables is constrained by the definition of a successful forecast. A duct forecast was considered to be successful if the lowest duct found in the observations was forecast by the model within a certain height threshold. A threshold of ± 50 m indicates that for a duct forecast to be successful the duct height in the COAMPS data has to be within ± 50 m of the lowest duct present in the observations (if any). Using this threshold value, we found that less than one-half of the ducts present in the observations are correctly forecast by COAMPS (hit rate of 0.38). This means that COAMPS misses $\sim 62\%$ of the ducts seen in the observations and that $\sim 81\%$ of ducts forecast by COAMPS do not materialize. The probability of detection when using this threshold is close to 12%.

Figure 7 shows the curves of the contingency statistics as a function of different duct height thresholds. As expected, when the threshold increases so does the probability of detection and hits, whereas false alarms decrease. When a threshold of ± 2000 m is reached the duct forecast becomes a binary solution

(yes or no).⁸ Haack et al. (2010) calculated contingency statistics using this method. In our study, the probability of detection using a ± 2000 -m threshold is close to 73% and the hit rate is 0.65. The false alarm decreases by ~ 40 percentage points from the maximum value reached at ± 50 m ($\sim 81\%$) to $\sim 41\%$. This value is larger than the value reported in Haack et al. (2010) (19% false alarm). The hit rate calculated in Haack et al. (2010) is 0.43, whereas in our study it is 0.65. This makes the discrimination score a value of 0.24, which is comparable to the Haack et al. (2010) value of 0.25. The differences in their values may be due to the nature of the observations and the number of ducts observed.

In our study, the discrimination score substantially decreases if the threshold decreases because the definition of a successful duct forecast becomes more restrictive. When the duct height threshold is ± 50 m, the discrimination score is -0.43 , which indicates that the false-alarm rate is larger than the hits. This emphasizes again the restrictions when evaluating features such as ducts, which are the product of unique meteorological setups.

The definition of a successful duct forecast can become more complicated as more variables come into play, such as duct strength and duct duration or accounting

⁸ Because we looked for electromagnetic ducts within the first 2000 m.

for ducts at different altitudes. In our study, we see that up to when the false-alarm rate is larger than the hit rate, an approximately ± 250 -m threshold, the quantification of the contingency statistics become too strict for the numerical model to keep up⁹ (Fig. 7). In our study, we conclude that both Fig. 6 and Fig. 7 show that COAMPS is able to reproduce the location of the ducts, especially since many of the ducts occur below 1000 m (Fig. 6). In addition, the model is limited by its vertical resolution. For example, if an intermediate threshold is used (above ± 400 m), this would allow the model to have between six and eight vertical levels at which the duct can be located, and in this case the probability of detection is close to 57% and the hits are $\sim 58\%$.

b. Mean EM properties during CASPER East

Figure 8 shows the mean characteristics of the ducts with duct height below 2000 m during the CASPER period. Figure 8a shows the percentage of the time that ducts were found at each location. The frequency of ducts varies depending on the region. The main CASPER observation region (offshore Duck) has the greatest percentages, between 60% and 65%, for both land and ocean. Figure 8a also shows more-frequent ducts over land than over the ocean, especially southwest of Duck. The frequency of ducts decreases slowly eastward from longitude 75.2°W. The region of higher frequency of ducts is also constrained by the SST gradients. The number of ducts with height ≤ 2000 m decreases considerably at the edge of the narrow SST gradient that forms between the coast and the Gulf Stream (Fig. 8a, gray contours). Southeast of the SST front region, the EM ducts decrease to $\sim 45\%$; in this area the mean SSTs are warmer (~ 300 K).

The ducts with maximum strength are offshore Duck with mean strength of values of $\sim 14 M$ units (see Fig. 8b). The ducts that formed over the ocean have greater intensity than those formed over land (Fig. 8b). The weakest ducts over the ocean are located close to the SST gradient. The distribution of the mean duct height is very different from the distribution of duct strength. The duct height appears to be more linked to the location of the duct while it is not necessarily true that the deeper ducts are stronger than the shallower ducts (see Fig. 8c). The deeper ducts, however, tend to be thicker than the shallower ducts (not shown), with the exception of an area northeast of Duck where the duct heights are low between 700 and 800 m and the duct thickness is close to 250–270 m in depth (not shown).

The mean duct height increases farther away from the coast. This may be because of the boundary layer height and its tendency to increase over the warmer ocean temperatures rather than over the land. The mean duct height close to Duck is ~ 700 m and increases at a rate of about $\sim 3 \text{ m km}^{-1}$ eastward until reaching a maximum of ~ 1300 m over the southeastern corner of the model domain (see Fig. 8c).

The location of the maximum standard deviation in duct height is close to the location in minimum in duct strength, and where the SST front associated with the Gulf Stream is located (see Fig. 8d). This may be associated with day-to-day variations in the location of the Gulf Stream or could also be related to the direction of the surface winds relative to these waters. Figure 8d also shows the standard deviation of SSTs over the region. The areas with the maximum variations of duct height (Fig. 8d) and minimum duct strength (Fig. 8b) are in the region with the greatest changes in SSTs. The mean SST deviations in those regions are greater than 1 K (see Fig. 8d, blue lines). This may be due to the nonuniform oceanographic and atmospheric characteristics in the region above the SST gradient.

The characteristics of ducts over land and over ocean are different. However, most of the EM ducts occur below 2 km over both land and ocean (99.2% and 97.38%, respectively). During CASPER EM ducts over the ocean were higher and stronger than those over land; however, there are some land areas close to the coast that have ducts more frequently than in the ocean. Based on the COAMPS forecasts, the mean duct height over the ocean (land) was 867.7 m (579.1 m) with a mean trapping layer at 751.5 m (473.4 m) and mean duct strength of 11.7 M units (10.7 M units).

The mean daily evolution of the ducts during the 24 days of CASPER East was also evaluated using COAMPS data.¹⁰ Duct height is observed to have a diurnal cycle, which is different over land than over the ocean. Figure 9 shows the joint probability density function of duct height for all land (Fig. 9a) and ocean (Fig. 9b) grid points in COAMPS.

The diurnal cycle over land is more pronounced than over the ocean, with the highest percentages at $\sim 28\%$. The duct height is lowest starting at ~ 2000 local time (LT) (between 0 and 100 m). Local time was used instead of UTC in Fig. 9 to get a sense of the daily duct evolution along with the known daily thermodynamic

⁹ Because the probability of detection is less than 50%.

¹⁰ The sounding data were not used because the sampling times throughout the experiment were different for most of the days and the amount of observations at different times of the day are not uniform.

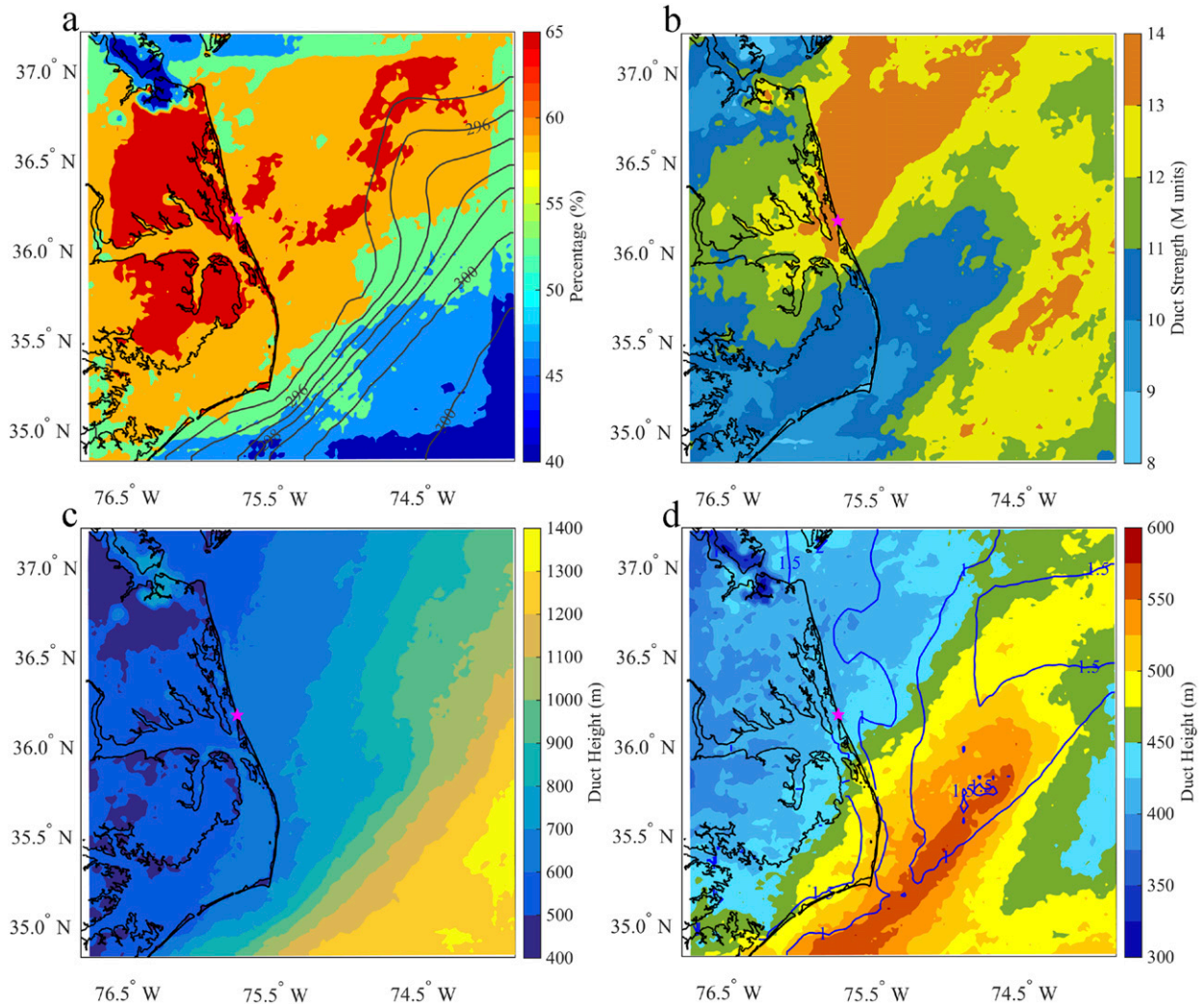


FIG. 8. Mean EM properties during CASPER East for the lowest electromagnetic duct with height ≤ 2000 m: (a) duct-presence percentage (the gray contours are the mean sea surface temperature during the CASPER period; plotted values are greater or equal to 295 K), (b) duct strength (M units), (c) duct height (m), and (d) mean standard deviation of duct height (m; filled contours). In (d), the blue contour lines are the SST standard deviation during CASPER (values plotted are ≥ 1 K). The magenta star marks the location of the pier at Duck.

variations (sunrise and sunset). The majority of the duct heights remain low up to 0600 LT and then increase. There is a gradual increase of duct height after sunrise hours (0700 LT), and this gradual increase continues up to 1400 LT; at this time there are three maxima of 15.7%, 11.2%, and 12.4% between 400 and 700 m. After this time the duct height decreases for most of the cases. Between 1600 and 1700 LT there is a maximum between 0 and 100 m of about 13.9%; there are also two other maxima between 400 and 500 m and between 800 and 900 m of 11.2% for each. This result indicates that for some of the cases the ducts can be formed close to the surface or keep growing as in the previous hours. After sunset (~ 1800 LT) the percentage of ducts closer to the

surface increases to 18.8% (see Fig. 9a). At this time there are also maxima between 800 and 900 m (13.1%) and between 1100 and 1200 m (10.6%). After 2000 LT the greatest duct height percentages are for those ducts closer to the surface.

The joint probability density function for all of the ocean points shows a very different diurnal evolution than for those over land. In this case there is not much variation during the day (see Fig. 9b). Overall the ducts that develop over the ocean are higher than those over land. There are two peaks within the first 2000 m: between 100 and 700 m and a thin layer between 1100 and 1200 m (see Fig. 9b). The percentage of ducts that fall in these heights varies during the day, but ranges between

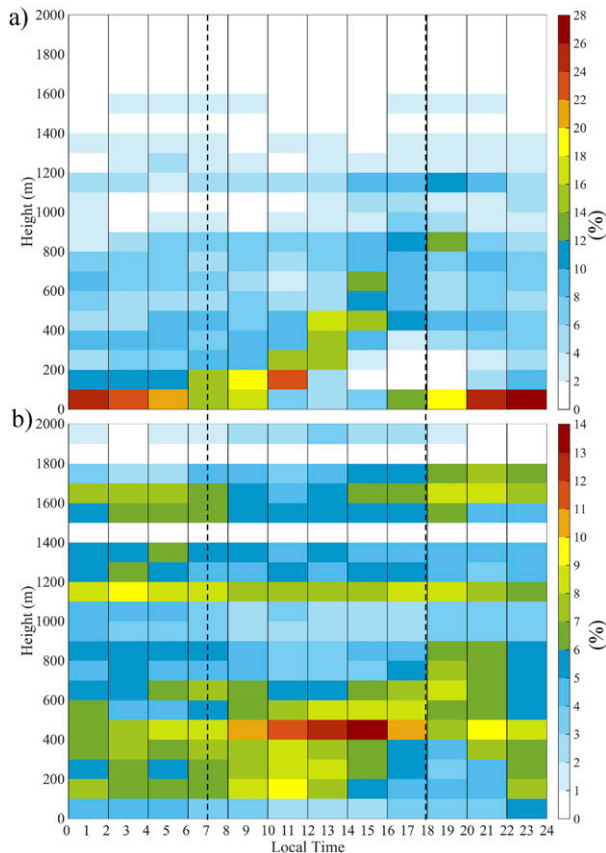


FIG. 9. Joint probability density function of duct height vs local time for ducts with duct height ≤ 2000 m for (a) land and (b) ocean grid points. The local time used is UTC $- 4$ h, since the majority of the observations were taken during October. The bin size is 100 m for the duct height and 2 h for the local time. The percentage corresponds to the distribution of ducts in the vertical direction for all points over land or ocean at each hour. The sum of all percentages in height for each time bin is 100%. The dotted lines represent the sunrise and the sunset average time during the period: 0705 and 1803 LT, respectively. The number of land and ocean grid points in the COAMPS domain is 3702 and 13 198, respectively, which corresponds to 21.9% and 78.1%, respectively, of the total domain.

5% and 14%. There is also a third peak around 1500–1700 m, which disappears between 0800 and 1800 LT and appears again after 1800 LT. During these hours most of the ducts form between 400 and 500 m. There is also a slight increase in duct height after 1800 LT, and for the next 2 h the ducts form higher (see Fig. 9b).

Figure 10 shows the mean COAMPS evaporative duct height and the evaporative duct height histogram along the CASPER track. Table 3 shows statistics calculations that are based on the histograms shown in Fig. 10 for each selected location and as a mean for all domain points. There is an increase of the evaporative duct height offshore as SST increases (Fig. 10a), similar to the surface-based or elevated duct (Fig. 8c). From Fig. 10 we can see

that the peak duct height moves toward higher values for locations that are farther offshore (east) (Fig. 10b). For most of the selected locations, the distribution shows a bimodal shape, with a second maximum ~ 5 m larger than the first. The first maximum for the three locations closest to the coast is at 5 m; the second maximum is between 8 and 10 m in the locations closest to the coast. The histograms start to differ as the distance from the coast increases. The R62 and R90 histograms seem to be shifted to the higher evaporative duct heights. R90 is still mostly bimodal, with the first maximum close to 12 m and the second one at around 13 m. This trend of increasing evaporative duct height as one moves away from the coast is evident when the mean evaporative duct height is calculated. At R02, R16, and R30 the mean values are 8.01, 8.85, and 8.95 m, respectively, whereas at R62 and R90 the mean values are 11.15 and 13.34 m, respectively. The R02 histogram differs statistically from the other histogram (see Table 3). It has the highest values of kurtosis (25.76), skewness (3.08), and variance (18.28), which means that the distribution is heavily tailed and highly asymmetric. This difference is possibly due to its closeness to the coast (2.04 km). This will translate to larger evaporation duct changes as a result of landmasses interacting with the ocean. This effect seems to be minimized by 30 km offshore at R30, which has a much lower variance, kurtosis, and skewness. R16 also shows large kurtosis and variance values, as well as positive skewness. In this case, these may be due to its closeness to the SST gradients, which will have an effect on the evaporation duct formation in the region, and especially its variations (variance = 16.54). R16 and R30 are also skewed to lower evaporative duct height values, whereas R62 and R90 are clearly skewed to larger evaporative duct height values (Table 3; Fig. 10b).

The mean evaporative duct height obtained from the observations (vertical gray line in Fig. 10b) is between the value calculated at R30 and R62: 11.92 m. The mean evaporative duct height for the entire region (black line on Fig. 10b; Table 3) is 10.48 m (black star in Fig. 10b). No diurnal cycle variations were found when calculations over the entire domain were performed.

c. Case study

The date of 20 October 2015 was chosen to study in greater detail (shaded area in Fig. 3). During this period, COAMPS verified reasonably well in representing the EM ducts and had a large number of observations. Conditions on this day were cooler and drier than the mean conditions during CASPER because of the passage of a cold front three days earlier (17 October). Figure 11 shows the COAMPS time series of water vapor mixing ratio, potential temperature, and wind speed

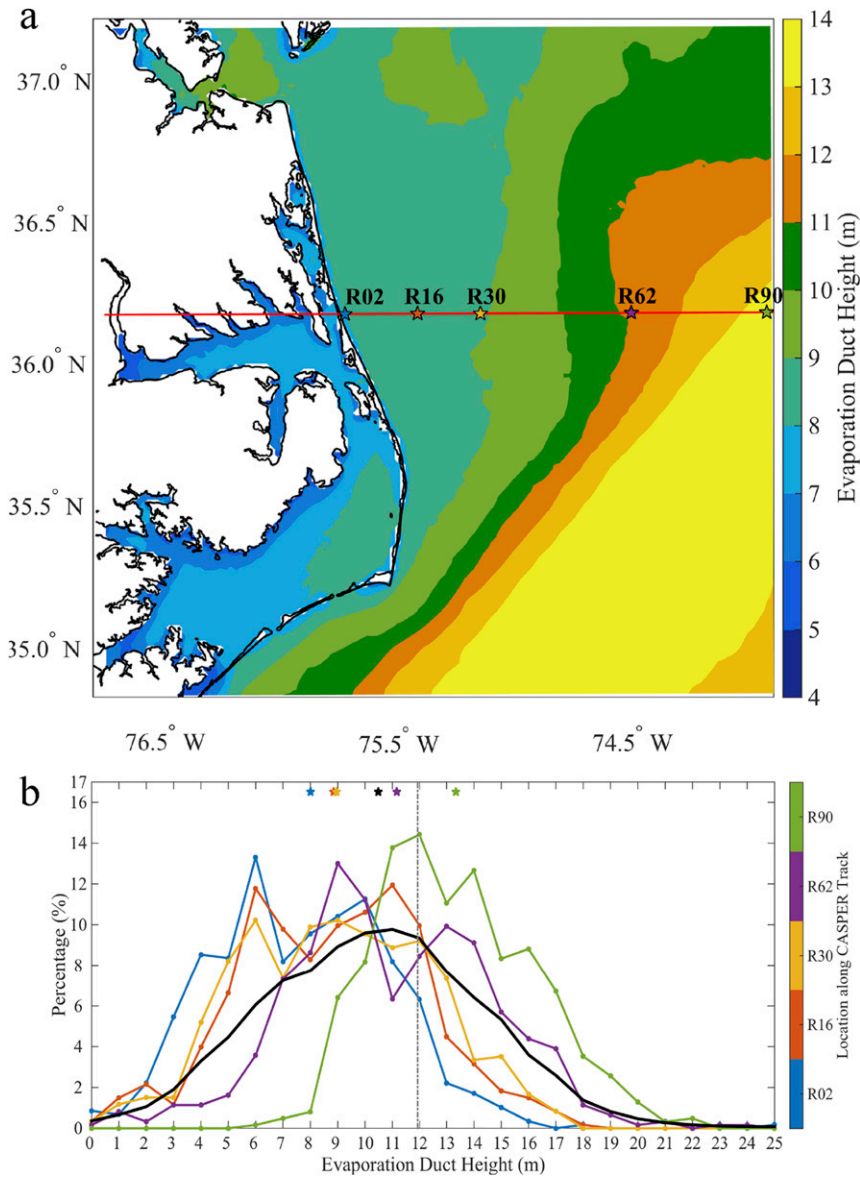


FIG. 10. (a) Mean evaporative duct height (m), and (b) histogram of evaporative duct height at different locations. The red line in (a) is the CASPER track (along 36.18°N); each star represents a location (by longitude) along the track: R02 (75.73°W), R16 (75.41°W), R30 (75.14°W), R62 (74.48°W), and R92 (73.88°W). Each line in (b) is the histogram at one of those locations along the CASPER track, as indicated by the color bar. The stars at the top of (b) are the mean evaporative duct height at each location. The black curve in (b) is the histogram for all ocean points in the COAMPS domain. The vertical dotted gray line in (b) represents the mean value of the evaporative duct height that was deduced from the tethered-balloon observations: 11.92 m.

for a location ~54.31 km offshore Duck (see Fig. 8a). Colder temperatures occur after 17 October 2015. During 20 October 2015, the potential temperature close to the surface reached values of ~278 and 288 K close to 1000 m. After 19 October 2015, the temperatures warm again, beginning with the upper levels (Fig. 11a). Thus, this case study takes place during the warming period.

Cold fronts are typically associated with a drier atmosphere and a decrease in the number of ducts (Babin 1995). In this case the values of water vapor mixing ratio are less than 6 g kg^{-1} close to the surface and less than 1 g kg^{-1} around 2000 m. Dry conditions persisted for 3 days. After midday during 20 October 2015, the humidity values are close to what they were before the cold-frontal passage.

TABLE 3. Evaporative duct height histogram function statistics for each location in Fig. 10 and for all domain (ocean) points.

Location	R02	R16	R30	R62	R90	All
Distance from coast (km)	2.04	30.66	55.19	114.47	167.62	
Mean	8.01	8.85	8.96	11.16	13.34	10.48
Variance	18.28	11.25	12.01	16.54	7.90	18.80
Kurtosis	25.76	2.73	2.04	10.22	2.70	7.57
Skewness	3.08	-0.06	-0.02	1.20	0.37	0.90

During this period there was also a very rapid decrease in wind speed. Between 18 and 19 October an intensification of the winds occurring within the lowest 2000 m of the atmosphere is associated with the frontal passage. By 20 October 2015 the wind magnitude is relatively low within the lowest 1500 m (below 2 m s^{-1}), which is in sharp contrast with the values of greater than 10 m s^{-1} one day earlier

(19 October; see Fig. 11c). During this time period COAMPS forecasts of duct height agreed with observations very well (see Figs. 11a–c). In total there were 21 soundings on 20 October 2015. All soundings were launched between the pier at shore and up to $\sim 80 \text{ km}$ offshore, where the SST ranges between 291 K (close to coast) and 293 K ($\sim 80 \text{ km}$ offshore) (see Fig. 12).

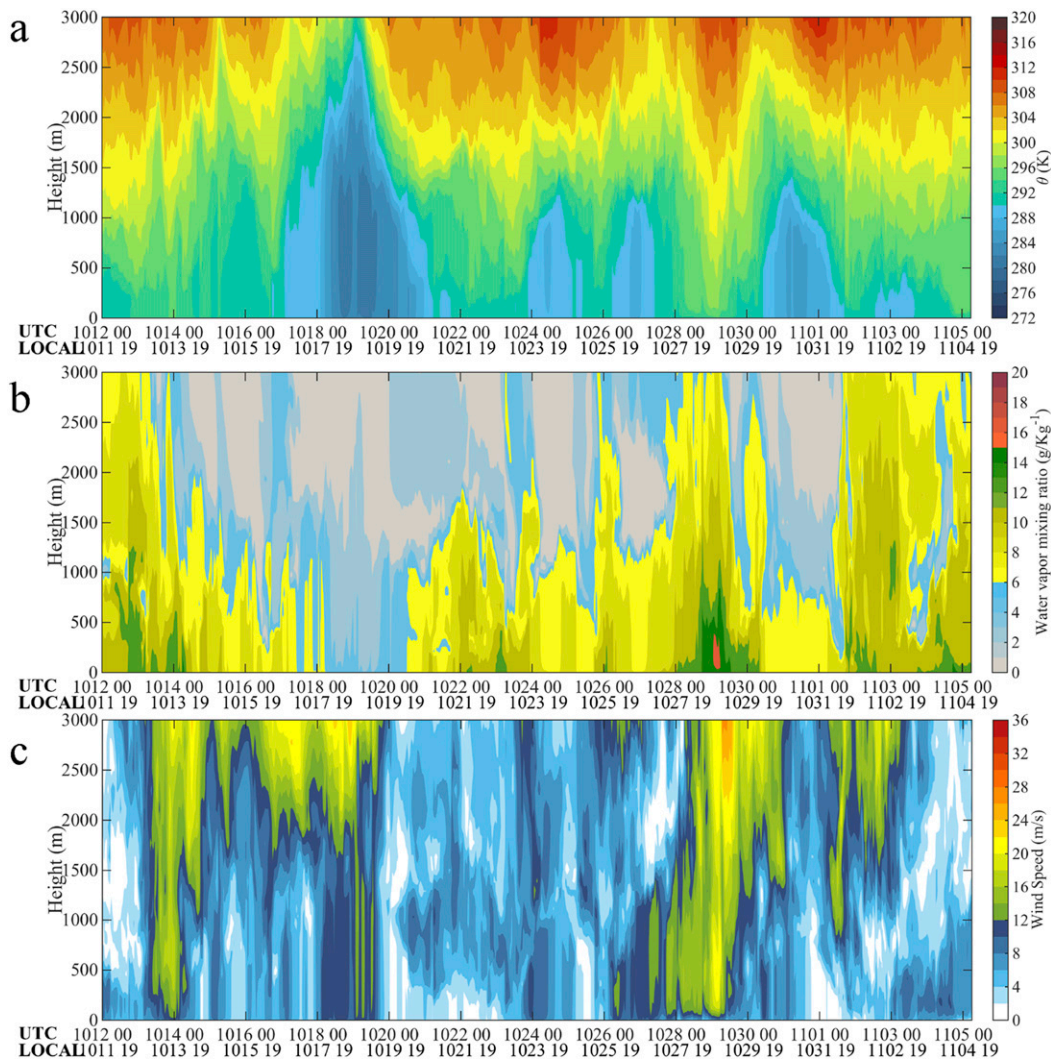


FIG. 11. Height (m) vs time for COAMPS (a) potential temperature (K), (b) water vapor mixing ratio (g kg^{-1}), and (c) wind speed (m s^{-1}) at location R30 offshore Duck (see Fig. 10a).

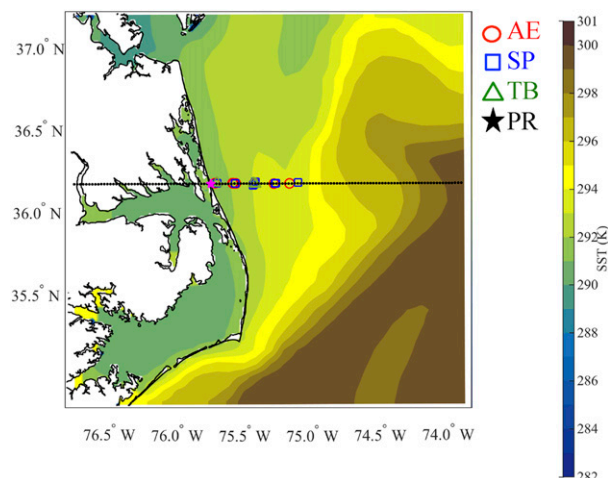


FIG. 12. Mean SST during the case on 20 Oct 2015. The circles and squares denote the locations of the soundings taken from RVAE and RVHRS. The triangles denote the location of the tethered balloon. The star denotes the location of the pier at Duck.

Figure 13 shows the longitudinal cross sections (height vs distance from coast) along the CASPER track. At late hours of the day (LT), the coastal regions are characterized mainly by surface-based ducts (Figs. 13a,b) and a secondary duct elevated around 1000 m, which gradually diminishes with time. At 0200 UTC (2200 LT) there are elevated ducts over the ocean (~1-km elevation) with the duct height increasing with distance away from the coast (to the east) (Fig. 13a), which is a pattern that was often evident during the experiment (Fig. 8c). The duct height (duct top) over the ocean and the elevated ducts over land are near the inversion layer.

The surface-based ducts along the coast are related to the cooler and drier conditions over land. There is a clear divide between the coastal layer and the marine layer. The marine layer, even at early hours of the day, is moister and more well mixed than over the coast. Holt and Raman (1992) and Herbster (1990) observed similar variations in the turbulence and the MABL structure above SST fronts from aircraft data. The increase of the SST can be clearly seen in the SST profile plotted below Fig. 13a.

The strong division between continental and marine air masses is more evident when examining the water vapor mixing ratio longitude–height cross section (Fig. 14). Above the ocean the boundary layer is moister and higher. There are also signs of low-level convergence with associated updrafts close to the coast between 0000 and 0400 UTC; at 0200 UTC (Figs. 13a and 14a) the convergence has reached approximately 18 km offshore up to 800 m. This convergence zone moves to the east over the next several hours until it is eventually well offshore. By 1500 UTC the duct layer has extended close to 80 km offshore and the convergence zone is no longer in the picture

(see Figs. 13d and 14d). The penetration of this duct layer from the coast to the MABL is clear at 1700 UTC where the duct layer has invaded well within the moist layer above the SST front (Fig. 14e). Five hours later, the air temperature starts to increase and the penetrating duct layer disappears, leaving the usual sloped duct layer seen during most of the experiment (Figs. 13f and 14f).

This sloped inversion layer and the EM ducts that are associated with it (Fig. 13) have been observed in past studies (Thompson and Haack 2011). In this case the continental air is advecting offshore. As this occurs, the surface-based ducts along the coast grow deeper. Around 1700 UTC, the continental boundary layer is immersed within the MABL, reaching up to 80 km offshore (Fig. 13e). After this, it starts retreating, decreasing the duct heights close to the coast (Fig. 14f). The movement of the continental air within the marine layer changes the duct distributions in the region. The ducts that were close to the coast at the beginning slope upward following the pattern of the inversion layer. The immersion of the coastal air into the marine air strengthens the ducts that remain close to the coast, especially after 1500 UTC (see Figs. 13d–f and 14d–f).

Another feature seen during this case study is a small (25-km horizontal extent) overturning cell in the wind pattern with downward motion at ~43 km offshore and upward motion at ~67 km offshore around 0200 UTC. The vertical extent of this small circulation cell reaches up to 800 m (see Figs. 13a and 14a). The location of this circulation is related to an increase in SSTs close to the location of the Gulf Stream (see Fig. 13a). This convergence region moves east over the next few hours (87 km at around 0300 UTC; 96 km at 0400 UTC) and disappears after that. At 2000 UTC (not shown) it appears again at ~160 km from the coast and moves westward with time: 122 km at 2100 UTC, 100 km at 2200 UTC (see Fig. 13f), and roughly 87 km around 2300 UTC.

During CASPER East there were other interesting days on which specific large-scale conditions created an interesting EM pattern. One of those cases is 1 November 2015. During this day ducts formed sloping upward toward the warmer SSTs close to the Gulf Stream. The wind pattern also followed the sloped shaped of the inversion (not shown). Stronger ducts are also evident above the warmer SSTs. As time progresses, the wind magnitudes in the lower levels decrease (increase) in the cooler (warmer) side of the SSTs and there is a clear change in the wind direction (and speed) on top of the SST front.

4. Conclusions and summary

In this study we used COAMPS simulations to describe the mean EM properties during the

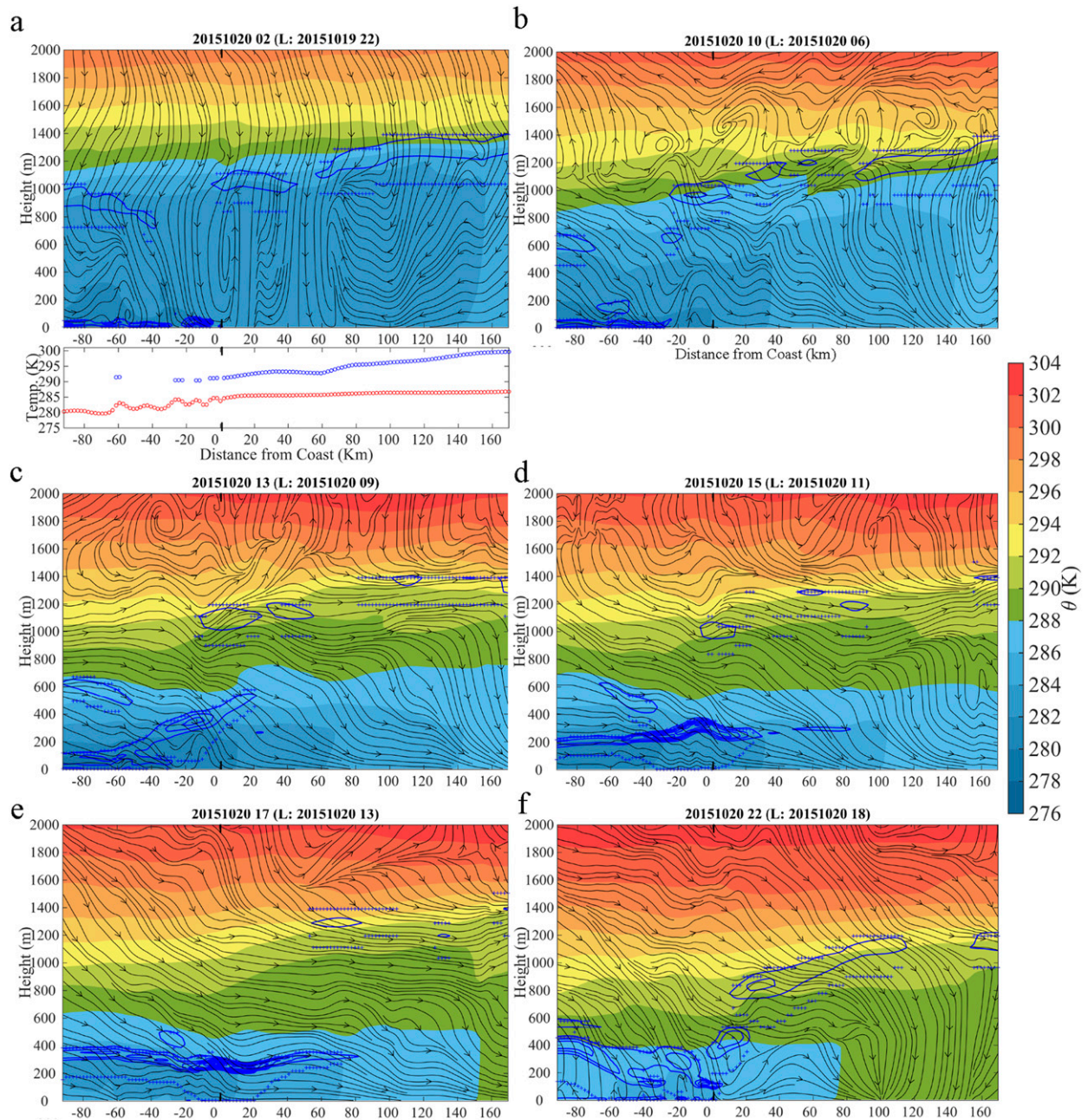


FIG. 13. Height (m) vs distance from the coast (km) along the CASPER track and ~80 km inland for different hours during 20 Oct 2015: (a) 0200, (b) 1000, (c) 1300, (d) 1500, (e) 1700, and (f) 2200 UTC. The ocean (blue circles) and the air (red circles) temperatures are given below (a). The blue contours are the negative values of dM/dz plotted every 0.1 M units m^{-1} ; the blue plus signs denote the duct-base height and duct height for each duct. The filled contours are the potential temperature plotted every 2 K; the wind streamlines (u, w) are plotted in black. The values of w were scaled by a factor of 233.97. This factor is the absolute value of the total mean of the zonal wind (1.56 m s^{-1}) divided by the total mean of the vertical wind (-0.01 m s^{-1}) during the case study and for all vertical levels.

CASPER field campaign. Our results show that COAMPS performed well in forecasting the meso-scale and EM conditions during the experiment. This was tested using four different sources of

observations: sounding, bow-mast, tethered-balloon, and SST data.

The six main EM properties observed during the CASPER period are

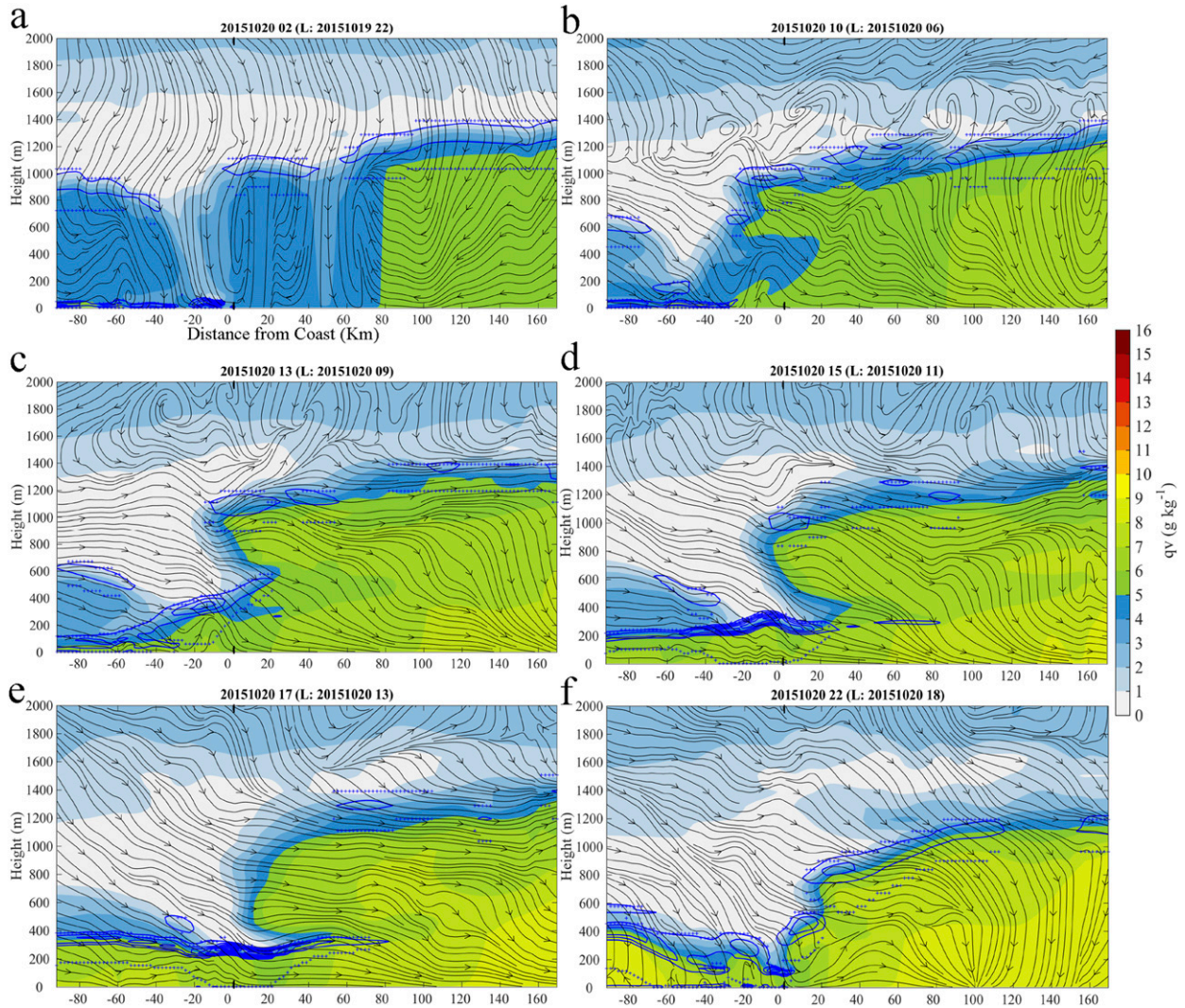


FIG. 14. As in Fig. 13, but the filled contours are water vapor mixing ratio plotted every 2 g kg^{-1} .

- 1) the duct frequency decreases and height increases farther away from the coast,
- 2) the spatial extent of the duct strength is seen to be limited by the SST front,
- 3) there is a diurnal evolution of the duct height over land,
- 4) the ducts over land are more frequent than over the ocean,
- 5) the ducts over the ocean are stronger and deeper than those over land, and
- 6) the evaporation duct height increases offshore the coast.

The evolution of the duct height and strength during most of the period was similar to the 20 October case in which surface-based ducting dominated near the coast and during the day, extending and deepening offshore. However, there are other cases in which the ducts

became shallower over the ocean as a result of the passage of different air masses (1 November).

The CASPER East period was characterized by very rapid changes in ducting conditions that occur in this near-shore environment associated with mesoscale flow. Therefore, this emphasizes the necessity of using an accurate high-resolution mesoscale model such as COAMPS to capture this variability, especially since single-point observations do not reflect the overall ducting conditions in the region.

Acknowledgments. Ulate, Wang, and Alappattu acknowledge the funding support for Coupled Air–Sea Processes and Electromagnetic Ducting Research (CASPER) by the Office of Naval Research (ONR) under its Multidisciplinary University Research Initiative (MURI) program (Grant N0001418WX01087). Haack and Holt were funded under the ONR Project N0001417WX02083. The

authors thank the anonymous reviewers for their input that helped to improve this paper.

REFERENCES

- Alappattu, D. P., Q. Wang, and J. Kalogiros, 2016a: Anomalous propagation conditions over eastern Pacific Ocean derived from MAGIC data. *Radio Sci.*, **51**, 1142–1156, <https://doi.org/10.1002/2016RS005994>.
- , —, R. Rainer, R. Yamaguchi, and R. J. Lind, 2016b: Characteristics of surface layer scalar profiles using the in-situ measurements from an undisturbed marine environment. *20th Conf. on Air–Sea Interaction*, Madison, WI, Amer. Meteor. Soc., 4.4, <https://ams.confex.com/ams/21SATMET20ASI/webprogram/Paper297336.html>.
- , —, R. Yamaguchi, R. J. Lind, M. Reynolds, and A. J. Christman, 2017: Warm layer and cool skin corrections for bulk water temperature measurements for air–sea interaction studies. *J. Geophys. Res. Oceans*, **122**, 6470–6481, <https://doi.org/10.1002/2017JC012688>.
- Babin, S. M., 1995: A case study of subrefractive conditions at Wallops Island, Virginia. *J. Appl. Meteor.*, **34**, 1028–1038, [https://doi.org/10.1175/1520-0450\(1995\)034<1028:ACSOSC>2.0.CO;2](https://doi.org/10.1175/1520-0450(1995)034<1028:ACSOSC>2.0.CO;2).
- , 1996: Surface duct height distributions for Wallops Island, Virginia, 1985–1994. *J. Appl. Meteor.*, **35**, 86–93, [https://doi.org/10.1175/1520-0450\(1996\)035<0086:SDHDFW>2.0.CO;2](https://doi.org/10.1175/1520-0450(1996)035<0086:SDHDFW>2.0.CO;2).
- , G. S. Young, and J. A. Carton, 1997: A new model of the oceanic evaporation duct. *J. Appl. Meteor.*, **36**, 193–204, [https://doi.org/10.1175/1520-0450\(1997\)036<0193:ANMOTO>2.0.CO;2](https://doi.org/10.1175/1520-0450(1997)036<0193:ANMOTO>2.0.CO;2).
- Bean, B. R., and E. J. Dutton, 1966: *Radio Meteorology*. Dover Publications, 435 pp.
- Burk, S. D., and W. T. Thompson, 1997: Mesoscale modeling of summertime refractive conditions in the Southern California Bight. *J. Appl. Meteor.*, **36**, 22–31, [https://doi.org/10.1175/1520-0450\(1997\)036<0022:MMOSRC>2.0.CO;2](https://doi.org/10.1175/1520-0450(1997)036<0022:MMOSRC>2.0.CO;2).
- Fairall, C. W., E. F. Bradley, J. E. Hare, A. A. Grachev, and J. B. Edson, 2003: Bulk parameterization of air–sea fluxes: Updates and verification for the COARE algorithm. *J. Climate*, **16**, 571–591, [https://doi.org/10.1175/1520-0442\(2003\)016<0571:BPOASF>2.0.CO;2](https://doi.org/10.1175/1520-0442(2003)016<0571:BPOASF>2.0.CO;2).
- Fu, Q., and K. Liou, 1993: Parameterization of the radiative properties of cirrus clouds. *J. Atmos. Sci.*, **50**, 2008–2025, [https://doi.org/10.1175/1520-0469\(1993\)050<2008:POTRPO>2.0.CO;2](https://doi.org/10.1175/1520-0469(1993)050<2008:POTRPO>2.0.CO;2).
- Haack, T., C. Wang, S. Garret, A. Glazer, J. Mailhot, and R. Marshall, 2010: Mesoscale modeling of boundary layer refractivity and atmospheric ducting. *J. Appl. Meteor. Climatol.*, **49**, 2437–2457, <https://doi.org/10.1175/2010JAMC2415.1>.
- Herbster, C. G., 1990: The vertical structure of the marine atmospheric boundary layer across a sea surface temperature front. Atmospheric Boundary Layer Group Tech. Rep., 164 pp., <https://apps.dtic.mil/dtic/tr/fulltext/u2/a227931.pdf>.
- Hodur, R. M., 1997: The Naval Research Laboratory’s Coupled Ocean/Atmosphere Mesoscale Prediction System (COAMPS). *Mon. Wea. Rev.*, **125**, 1414–1430, [https://doi.org/10.1175/1520-0493\(1997\)125<1414:TNRLSC>2.0.CO;2](https://doi.org/10.1175/1520-0493(1997)125<1414:TNRLSC>2.0.CO;2).
- Holt, T. R., and S. Raman, 1992: Three-dimensional mean and turbulence structure of a coastal front influenced by the Gulf Stream. *Mon. Wea. Rev.*, **120**, 17–39, [https://doi.org/10.1175/1520-0493\(1992\)120<0017:TDMATS>2.0.CO;2](https://doi.org/10.1175/1520-0493(1992)120<0017:TDMATS>2.0.CO;2).
- Kang, D., and Q. Wang, 2016: Optimized estimation of surface layer characteristics from profiling measurements. *Atmosphere*, **7**, 14, <https://doi.org/10.3390/atmos7020014>.
- Khairoutdinov, M., and Y. Kogan, 2000: A new cloud physics parameterization in a large-eddy simulation model of marine stratocumulus. *Mon. Wea. Rev.*, **128**, 229–243, [https://doi.org/10.1175/1520-0493\(2000\)128<0229:ANCPPI>2.0.CO;2](https://doi.org/10.1175/1520-0493(2000)128<0229:ANCPPI>2.0.CO;2).
- Klemp, J., and R. Wilhelmson, 1978: The simulation of three-dimensional convective storm dynamics. *J. Atmos. Sci.*, **35**, 1070–1096, [https://doi.org/10.1175/1520-0469\(1978\)035<1070:TSOTDC>2.0.CO;2](https://doi.org/10.1175/1520-0469(1978)035<1070:TSOTDC>2.0.CO;2).
- Louis, J.-F., 1979: A parametric model of vertical eddy fluxes in the atmosphere. *Bound.-Layer Meteor.*, **17**, 187–202, <https://doi.org/10.1007/BF00117978>.
- , M. Tiedtke, and J. F. Geleyn, 1982: A short history of the operational PBL parameterization at ECMWF. *Workshop on Planetary Boundary Parameterization*, Reading, United Kingdom, ECMWF, 59–79, <https://www.ecmwf.int/node/10845>.
- Mellor, G., and T. Yamada, 1982: Development of a turbulence closure model for geophysical fluid problems. *Rev. Geophys.*, **20**, 851–875, <https://doi.org/10.1029/RG020i004p00851>.
- Meyer, J. H., 1971: Radar observations of land breeze fronts. *J. Appl. Meteor.*, **10**, 1224–1232, [https://doi.org/10.1175/1520-0450\(1971\)010<1224:ROOLBF>2.0.CO;2](https://doi.org/10.1175/1520-0450(1971)010<1224:ROOLBF>2.0.CO;2).
- Monin, A. S., and A. Obukhov, 1954: Basic laws of turbulent mixing in the surface layer of the atmosphere. *Tr. Geofiz. Inst., Akad. Nauk SSSR*, **24**, 163–187.
- Rutledge, S., and P. Hobbs, 1983: The mesoscale and microscale structure and organization of clouds and precipitation in midlatitude cyclones, VIII: A model for the “seeder-feeder” process in warm-front rainbands. *J. Atmos. Sci.*, **40**, 1185–1206, [https://doi.org/10.1175/1520-0469\(1983\)040<1185:TMAMSA>2.0.CO;2](https://doi.org/10.1175/1520-0469(1983)040<1185:TMAMSA>2.0.CO;2).
- Thompson, W. T., and T. Haack, 2011: An investigation of sea surface temperature influence on microwave refractivity: The Wallops-2000 experiment. *J. Appl. Meteor. Climatol.*, **50**, 2319–2337, <https://doi.org/10.1175/JAMC-D-10-05002.1>.
- Turton, J. D., D. A. Bennetts, and S. F. G. Farmer, 1988: An introduction to radio ducting. *Meteor. Mag.*, **117**, 245–254.
- Wang, Q., and Coauthors, 2018: CASPER: Coupled Air–Sea Processes and Electromagnetic Wave Ducting Research. *Bull. Amer. Meteor. Soc.*, **99**, 1449–1471, <https://doi.org/10.1175/BAMS-D-16-0046.1>.
- Wang, S., Q. Wang, and J. Doyle, 2002: Some improvement of Louis surface flux parameterization. *15th Symp. on Boundary Layers and Turbulence*, Wageningen, The Netherlands, Amer. Meteor. Soc., 13.3a, https://ams.confex.com/ams/BLT/techprogram/paper_44519.htm.
- , L. W. O’Neill, Q. Jiang, S. P. de Szoeke, X. Hong, H. Jin, W. T. Thompson, and X. Zheng, 2011: A regional real-time forecast of marine boundary layers during VOCALS-REX. *Atmos. Chem. Phys.*, **11**, 421–437, <https://doi.org/10.5194/acp-11-421-2011>.
- Wilks, D. S., 2011: *Statistical Methods in the Atmospheric Sciences*. 3rd ed. International Geophysics Series, Vol. 100, Academic Press, 704 pp.
- Zhang, Q., K. Yang, and Y. Shi, 2016: Spatial and temporal variability of the evaporation duct in the Gulf of Aden. *Tellus*, **68A**, 29792, <https://doi.org/10.3402/tellusa.v68.29792>.
- , —, and Q. Yang, 2017: Statistical analysis of the quantified relationship between evaporation duct and oceanic evaporation for unstable conditions. *J. Atmos. Oceanic Technol.*, **34**, 2489–2497, <https://doi.org/10.1175/JTECH-D-17-0156.1>.